Chemical Engineering Journal 499 (2024) 155971

Contents lists available at ScienceDirect

Chemical Engineering Journal

journal homepage: www.elsevier.com/locate/cej

Optimal carbofuran degradation via CWPO in NOM-doped water by a framework Cu-doped aluminate perovskite catalyst derived from aluminum saline slags

H.J. Muñoz [a], L.A. Galeano [b], M.A. Vicente [c], S.A. Korili [a], A. Gil [a,*]

[a] INAMAT^2-Departamento de Ciencias, Edificio de los Acebos, Universidad Pública de Navarra, Campus Arrosadia, 31006 Pamplona, Spain
[b] Grupo de Investigación en Materiales Funcionales y Catálisis, Departamento de Química, Universidad de Nariño, Calle 18, Cra 50 Campus Torobajo, 520002 Pasto, Colombia
[c] GIR-QUESCAT, Departamento de Química Inorgánica, Facultad de Ciencias Químicas, Universidad de Salamanca, 37008 Salamanca, Spain

ARTICLE INFO

Keywords:
$La_yAl_{1-x}Cu_xO_{3-\delta}$ perovskite catalyst
Saline slag
CWPO
Carbofuran
Multi-response statistical optimization

ABSTRACT

This study is the first to propose the synthesis of $La_yAl_{1-x}Cu_xO_{3-\delta}$ perovskite catalysts using Al recovered from acid leaching of saline slags. The effect of parameters such as the La/Al molar ratio was explored during the synthetic process. A suite of characterization techniques—including XRF, XRD, N_2 adsorption, H_2-TPR, FTIR, TGA-DTA, TEM, SEM, EDX, and XPS—confirmed the successful synthesis of high-purity (up to 90 %) perovskites with La and O vacancies, and a high concentration of Cu(I) active sites dispersed within the perovskite lattice. The best catalyst was used to optimize the degradation of carbofuran (CBF) in water doped with synthetic dissolved natural organic matter (NOM) using the Fenton-like catalytic wet peroxide oxidation (CWPO) approach. The effects of catalyst concentration, H_2O_2 dose, and pH on catalytic performance were investigated. Degradation, mineralization (COD removal), and H_2O_2 consumption were maximized, while Cu leaching was minimized using a statistical desirability function for multiple responses. Optimal conditions were found to be a catalyst concentration (mg Cu/mg H_2O_2) of 0.234 (2.0 g L^{-1}), an H_2O_2 dose of 73.3 % (0.73 times the stoichiometric dose for full COD mineralization), and a remarkable circumneutral pH of 6.2. Under these conditions, degradation reached 94.1 %, and COD mineralization was 51 % under room temperature. Notably, the perovskite catalyst exhibited remarkable stability during reuse in up to three cycles, as demonstrated by the low Cu leaching (<1.30 mg L^{-1}).

1. Introduction

The frequent detection of pesticides from both agrochemical companies and agricultural runoff in water supplies is a significant concern due to their high toxicity [1–4]. Carbofuran (2,3-dihydro-2,2-dimethylbenzofuran-7-yl methylcarbamate, CBF), a broad-spectrum carbamate insecticide and nematicide, has played a pivotal role in enhancing agricultural yields and securing food supplies by allowing effective control of various foliar pests in fruit, vegetable, and forest crops. However, its high water solubility (700 mg L^{-1}) and bio-refractory characteristics contribute significantly to pollution, thus posing a serious threat to aquatic ecosystems and human health [4,5].

CBF is also neurotoxic and has been linked to various health issues, such as dizziness, fatigue, respiratory illnesses, and even death [6,7]. Despite being banned in the United States and the European Union, recent research suggests that it is still used mainly in developing countries [8,9]. As such, efficient management of pesticide-containing industrial and agricultural wastewater before release into waterways or sewage systems is crucial. While traditional methods involving physical and chemical treatments have shown to be ineffective for persistent contaminants like CBF [1], the Fenton reaction, a powerful advanced oxidation process (AOP), appears promising due to its high efficiency, simplicity, and low environmental impact [10–13]. However, widespread application of the Fenton reaction is limited by its narrow effective pH range (2.5–3.5), sludge generation (primarily Fe-based, a secondary pollutant), and ongoing catalyst loss [10].

In the same way, aluminum saline slags, an unavoidable byproduct of the secondary Al production process, also raise growing

---

* Corresponding author.
E-mail address: andoni@unavarra.es (A. Gil).

https://doi.org/10.1016/j.cej.2024.155971
Received 2 July 2024; Received in revised form 28 August 2024; Accepted 18 September 2024

environmental and economic concerns. With an estimated accumulation of 4 to 5 million tons annually, these slags pose risks to public health and the environment due to their potential to generate flammable, toxic, and even explosive gases upon contact with water [14,15]. Furthermore, their storage in controlled landfills entails high costs and long-term environmental risks. The composition of saline slags, which include 3–9 % metallic Al, oxides, fluxing salts, and other components, complicates their management and valorization [16,17]. Indeed, the separation of these components for subsequent recovery and application is complex, costly, and energy-intensive and exerts considerable environmental impact. In this context, finding alternatives for the management, utilization, and recycling of saline slags has become an urgent necessity. Acidic extraction using HCl has been extensively studied as a potential method for extracting Al from saline slags [18–21]. This process of aluminum recovery and valorization of this hazardous residue contributes to environmental sustainability by reducing waste and minimizing the need for new raw materials, thereby decreasing the environmental footprint of the process [22,23]. Furthermore, the use of aluminum (Al) recovered from saline slags in the synthesis of new materials offers significant advantages in terms of energy efficiency compared to commercial Al, as the production of the latter may require energy-intensive methods involving high temperatures, additional chemical reactions, and elevated energy consumption [24]. Therefore, this reduction in energy demand not only lowers operational costs but also contributes to a smaller carbon footprint associated with the production of new functional materials [16,25,26]. Recently, Olivares *et al.* [27] demonstrated that the implementation of saline slags valorization process reduces the GWP (Global Warming Potential) by 13 tonnes of CO_2 equivalent/tonne of Al, also generating significant environmental benefits. In this sense, the synthesis of materials such as hexaaluminates [21], layered double hydroxides [28–30], zeolites [31,32], ceramic-MOF filters [33], and Al-pillared clays [20] has been reported using these saline slags. However, the current focus on using only the Al obtained in the first extraction overlooks the high Al content remaining in the saline slag residue.

The acidic treatment of these slags offers a novel opportunity to recover high value-added Al with minimal environmental impact, as an alternative source of Al in the synthesis of perovskite-type oxides, such as lanthanum aluminate ($LaAlO_3$). Due to its versatility in cationic substitution, this material can be modified with Cu to obtain $LaAl_{1-x}Cu_xO_{3-\delta}$, which exhibits unique physicochemical properties and holds great potential for various catalytic applications [10,34,35].

Cu-containing Fenton-like catalysts are garnering significant attention due to several advantages, such as easier Cu^{2+}/Cu^{+} cycling compared to Fe^{3+}/Fe^{2+} over a wider pH range, high natural abundance of Cu, and its lower cost [10,34,36–38]. This positions $LaAl_{1-x}Cu_xO_{3-\delta}$, a perovskite catalyst modified with Cu in the B-site, as a promising functional material. Furthermore, recent studies [39,40] suggest that La vacancies in this kind of catalysts can regulate the electronic structure of B-site metals and O atoms, potentially allowing optimization of the Fenton-like reaction. Moreover, $LaAl_{1-x}Cu_xO_{3-\delta}$ catalysts have demonstrated effective degradation of a wide range of persistent organic compounds, including diphenhydramine, ciprofloxacin, ibuprofen, phenytoin, and pesticides like 2-chlorophenol and 2,4-dichlorophenoxyacetic acid, even at near-neutral pH levels [10,34,41].

However, to the best of our knowledge, $La_yAl_{1-x}Cu_xO_3$ catalysts, taking advantage of Al extracted from saline slag residue (previously extracted with HCl), particularly those exhibiting La deficiency, have not been investigated for the degradation of pesticides such as CBF. This is especially relevant in matrices containing natural organic matter (NOM) that properly simulate real wastewater conditions. Municipal wastewater effluents typically exhibit a dissolved organic carbon (COD) content below 20 mg L^{-1} during dry weather and a near-neutral pH [42–46].

In light of the above, this study investigated the optimal conditions for maximizing CBF degradation in water containing a synthetic dissolved NOM using a Cu-modified perovskite catalyst prepared from Al extracted from saline slag residue. The catalytic wet peroxide oxidation process (CWPO) was employed, and a central composite statistical design of experiments (CCD) was used to assess the interactions between the main operational parameters, namely catalyst concentration, hydrogen peroxide dosage, and pH.

2. Experimental section

2.1. Materials and reagents

The materials were prepared using $La(NO_3)_3{\cdot}6H_2O$ (98 %, Acros Organics®), $Cu(NO_3)_2{\cdot}3H_2O$ (99 %, labkem®), citric acid ($C_6H_8O_7$)·H_2O, CA) (99 %, Opac S.A®) and HCl (37 %, Panreac®). The synthetic surrogate of surface water was prepared according to the procedure recently reported by García-Mora *et al.* [47] using poly(acrylic acid) (PAA, analytical grade Sigma-Aldrich, average MW 130,000 g mol^{-1}), poly(styrenesulfonate) in two molecular weights: 10^6 g mol^{-1} (PSS1, 25 wt%, Sigma-Aldrich), and 2×10^5 g mol^{-1} (PSS2, 30 wt%, Sigma-Aldrich), polygalacturonic acid (PGUA, > 90 wt%, enzymatic, Sigma-Aldrich, average MW 25,000 ~ 50,000 g mol^{-1}), and a commercial standard of humic acids (HA, analytical grade, Sigma-Aldrich). NaOH (99 %, Merck®) was used to enhance the solubility of PGUA and HA acids in water·H_2O_2 (30 %, Merck®), CBF (PESTANAL®, analytical standard), anhydrous Na_2SO_3 (97.0–100.5 %, Merck®) and HNO_3 (37 %, Panreac®) were employed in the CWPO catalytic tests.

2.2. Aluminum extraction

Al was extracted from the starting saline slag (W) using two consecutive extraction processes (Fig. S1). In each step, the slag (W) was treated with an aqueous solution of HCl (2.0 mol L^{-1}) under reflux at 100 °C for 2 h at a waste/volume (g mL^{-1}) ratio of 1:15 [20,21]. The resulting slurries were separated by centrifugation (Hettich ROTANTA 460 S) and dried at 60 °C before proceeding to the next extraction; the resulting materials were denoted as RW1 and RW2, respectively. The Al-containing solutions from each stage were labeled AH1 and AH2, respectively. The Al content in these solutions was determined by ICP-OES (Table 1).

2.3. Catalyst synthesis

$La_yAl_{1-x}Cu_xO_3$ perovskite composites (where y = 0.5, 0.75, and 1.0 and x = 0.0 and 0.05) were synthesized using the Pechini's process [48]. Lanthanum nitrate, copper nitrate, and citric acid (CA) were dissolved in deionized water (Solution A) followed by the dropwise addition of Al solution (AH2) with vigorous stirring (950 rpm). After stirring the resulting mixture at room temperature for 1 h, the solvents were evaporated at 80 °C to obtain a gel, which was then heated overnight at 200 °C. A CA/($Al^{3+} + La^{3+} + Cu^{2+}$) molar ratio of 3.0 was used to prepare the materials. Various $La^{3+}/(Al^{3+} + Cu^{2+})$ molar ratios (y = 0.5, 0.75, and 1.0) were evaluated. The resulting materials were ground and calcined at 950 °C. For clarity, the notation used for the pristine materials is La(y)AH2 and La(y)AH2-Cu for Cu-containing catalysts.

Table 1
Al content and density of the solutions obtained from consecutive acidic extractions.

Al solution	Al (g/L)[a]	Density (g mL^{-1})	Al recovery (%)[b]
AH1	4.94	1.06	NA
AH2	4.62	1.05	93.52

NA: Not applicable.
[a] Inductively coupled plasma (ICP) measurements.
[b] Recovery of aluminum relative to the first extraction (AH1), expressed as a percentage.

2.4. Physicochemical characterization

The chemical composition of the Al solutions was determined using inductively coupled plasma atomic emission spectrometry (ICP-AES) with a Varian ICP-OES instrument. Elemental analyses of the solid materials were performed semi-quantitatively using X-ray fluorescence (XRF) with a PANalytical AXIOS instrument equipped with a Rh anode as the X-ray source and three detectors (gas flow, scintillation, and Xe sealing). The powder X-ray diffraction (XRD) patterns were acquired using a BRUKER D8 Advance diffractometer at 40 kV and 25 mA, scanning speed of 2° (2θ)/min and CuKα filtered incident radiation ($\lambda = 1.5418$ Å). Textural analyses were conducted using the nitrogen adsorption–desorption isotherms measured at −196 °C in a Micromeritics ASAP 2020 Plus analyzer (150–200 mg of sample). The BET-specific surfaces (S_{BET}) were determined using the multipoint BET model and applying the Keii–Rouquerol criteria [49,50]. The total pore volume was estimated from the amount of adsorbed nitrogen at a relative pressure of $p/p^{\circ} = 0.98$, according to the Gurvitch method. H_2 temperature-programmed reduction analyses (H_2-TPR) were conducted using a Micromeritics TPR/TPD 2900 instrument. SEM (INSPECT F50, mode: 30 kV − map, detector: BSED) and TEM (FEI Tecnai F30, accelerating voltage: 200 kV, detector: HAADF-STEM) were used for the morphological and chemical composition analysis of the solids. Selected-area electron diffraction (SAED) experiments were performed using a Tecnai F30 (FEI) microscope. Infrared spectra of the samples were recorded using a JASCO FT/IR-4700 FT-IR spectrometer equipped with a diamond ATR accessory in a single-beam optical scheme. The spectra were obtained in the range 400 − 4000 cm^{-1} with a resolution of 4.0 cm^{-1}. Finally, X-ray photoelectron spectroscopy (XPS) data were obtained using a PHI VERSAPROBE II instrument, employing monochromatic Al Kα radiation (Al 1486.6 eV mono at 47.3 W). Deviations caused by electric charges on the samples were corrected using the C 1 s peak at 284.8 eV as an internal standard. Spectra were acquired with a pass energy of 29.3 eV.

$$CBFdegradation(\%) = \frac{initialconcentration\left(\frac{mg}{L}\right) - remainingconcentration\left(\frac{mg}{L}\right)}{initialconcentration\left(\frac{mg}{L}\right)}*100 \quad (1)$$

2.5. Synthetic surrogate

This experiment utilized a synthetic water surrogate mimicking the composition of agricultural wastewater. The surrogate was prepared by mixing specific volumes of commercially available standards selected based on their dissolved organic carbon percentages (see Table S1). Each standard represented a distinct polar fraction (hydrophilic, hydrophobic, or transphilic) [47,51–53]. Prior to mixing, each standard was dissolved in ultra-pure water. PGUA and HA acids required additional treatment with 2.0 mL of 0.3 mol L^{-1} NaOH solution. Once the synthetic water with NOM had been prepared (total COD concentration 17 mg_C L^{-1}), 3 mg_C L^{-1} of CBF was dissolved in this same solution, resulting in a total COD concentration of 20 mg_C L^{-1}.

2.6. Statistical multi-response optimization of the CWPO degradation of CBF

The catalyst concentration (mg Cu/mg H_2O_2), percentage of stoichiometric H_2O_2 dosage for COD oxidation, and the pH are important parameters in the Fenton-like CWPO process and, as such, were chosen as experimental factors [54]. The optimal conditions for CBF degradation in NOM-spiked water using the CWPO process were determined by performing 23 experiments arranged in a Central Composite Design (CCD). The levels of the experimental independent variables investigated (factors) are shown in Table 2.

Table 2
Statistical designs of experiments used to optimize main CWPO operating parameters in CBF degradation.

Experimental Variables	Levels		
	Low (−1)	High (+1)	Axial Points
Catalyst Concentration (mg Cu/mg H_2O_2)	0.050	0.187	0.003; 0.234
Stoichiometric H_2O_2 dosage(%)	40.0	80.0	26.4; 93.6
pH	3.0	7.0	1.6; 8.4

The response parameters were all analyzed at the final time of the CWPO reaction (3 h) as follows: *(i)* CBF degradation (pesticide removal, Eq. (1)); *(ii)* CBF and NOM mineralization (dissolved organic carbon removal, Eq. (2)); and *(iii)* fraction of consumed hydrogen peroxide (calculated from free peroxide concentration, Eq. (3)). The goal of the multi-response optimization was to simultaneously maximize *(i)*, *(ii)*, and *(iii)* while minimizing leached Cu concentration. The setup used for the catalytic assays is illustrated in Fig. S2.

Response surface methodology (RSM) was employed for single-response statistical optimization, followed by multi-response optimization using a desirability function normalized from each individual response optimum. The statistical significance of each term was assessed using the 95 % confidence level probability value (p-value) [47]. All statistical analyses were performed using Statgraphics software (version Centurion 19.6.02).

$$NOMmineralization(\%) = \frac{initialCOD\left(mg\frac{C}{L}\right) - remainingCOD\left(mg\frac{C}{L}\right)}{initialCOD\left(mg\frac{C}{L}\right)}*100 \quad (2)$$

$$H_2O_2consumed(\%) = \frac{fullH_2O_2added(mmol) - remainingH_2O_2(mmol)}{fullH_2O_2added(mmol)}*100 \quad (3)$$

2.7. Experiments of the CWPO removal of CBF

These catalytic experiments were conducted under atmospheric pressure (72 kPa) in a 500 mL jacketed glass semi-batch reactor equipped with continuous mechanical stirring of the reaction mixture (600 rpm) and temperature control using an external thermostatic bath ±0.1 °C) (Fig. S2). This catalytic test, adapted from García-Mora *et al* [47], involved dispersing the powdered perovskite catalyst (particle size ≤ 300 μm) in 250 mL of the initial water sample and maintaining continuous air bubbling (2.0 L h^{-1}) throughout. The pH was adjusted during the first 30 min of the experiment (prior to start the hydrogen peroxide addition) to achieve equilibrium between the solid and liquid phases. Subsequently, 60 mL of H_2O_2 solution were added gradually (0.33 mL min^{-1}) over 180 min of reaction time. The targeted dose of hydrogen peroxide was controlled based on the concentration of the added solution, while maintaining a constant volume. Samples (12 mL each time) were collected periodically during 4 h of each full experiment (30 min of equilibration → 3h of CWPO reaction → 30 min of final post-reaction stage, after the addition of hydrogen peroxide was complete). Each sample was microfiltered immediately (Millipore, 0.45 μm) after collection to determine pesticide degradation and COD. Excess, unreacted H_2O_2 was previously deactivated using methanol (642 μL) or sodium bisulfite (67 μL), depending on the case. The error introduced in the measurements due to NOM and CBF adsorption on the micro-filters was offset by applying an identical procedure to the starting water sample (zero reaction time) [47,55].

2.7.1. Analytical methods

The CBF concentration was determined by high-performance liquid chromatography (Shimadzu Prominence LC 20) using a C18 column (Luna Phenomenex, 250 mm × 4.6 mm, 5 μm) and a PDA detector at 40 °C. The mobile phase consisted of 50 % acetonitrile; 50 % Type I water:H_3PO_4 (pH 2.3) at a flow rate of 1 mL min^{-1}, with detection at 200 nm. COD concentrations were measured using a Shimadzu TOC-L apparatus (detection limit: 0.518 mg_C L^{-1}; quantification limit: 1.121 mg_C L^{-1}). COD removal reflected the combined mineralization of CBF and NOM. Free hydrogen peroxide concentrations were determined using the iodometric method at 361 nm (linear range: 0.0–15.0 mg L^{-1}; $R^2 = 0.999$; detection limit: 0.01 mg L^{-1}; quantification limit: 0.06 mg L^{-1}) [47,56]. Spectrophotometric measurements were conducted using a Shimadzu UV-2600 spectrophotometer. The catalyst was filtered after each experiment and its chemical stability was verified by determining the leached Cu concentration in the reaction effluent using atomic absorption spectroscopy on an ICE-3500 series 3000 spectrophotometer.

3. Results and discussion

3.1. Characterization of Al solutions and catalysts

The results of Al extraction from the saline slag using the two-step acid leaching process are summarized in Table 1. These results demonstrate the effectiveness of this process for the extraction of Al from the slag. AH2 achieved an Al recovery rate of 93.52 % compared to AH1, which points to the high potential for recovery of the metal from this waste material. Furthermore, a comparison of the XRF results for the starting saline slag (W) with the slag residues after the first (RW1) and second (RW2) acid extractions (Tables S3, S4, S5) showed significant changes in the chemical composition of the slag before and after treatment. Specifically, the weight percentage of Al_2O_3 increased considerably after each treatment (from 54.08 % to 65.89 % in RW1 and from 65.89 % to 75.26 % in RW2), thus suggesting effective Al extraction at each stage. This increase in Al_2O_3 content in RW1 and RW2 is also related to the removal of other oxides present in the starting slag (W), such as Fe_2O_3, CaO, K_2O, Na_2O, CuO, and Cl, amongst others, during the extraction process. These results are consistent with previous studies [21]. The densities of AH1 and AH2 were very similar (1.05 g mL^{-1}), thus indicating comparable concentrations of dissolved solids in both solutions. However, the XRD results (Fig. 1a) showed that using AH2 in the preparation of the perovskite with an La/Al molar ratio of 1 (La(1.0) AH2) leads to the formation of La_2O_3 (JCPDS # 96-101-0279) impurities in addition to the perovskite, with an XRD pattern that coincides with the theoretical one (JCPDS #96-220-6577). Thus, introducing Cu into La (1.0)AH2 to form La(1.0)AH2-Cu resulted in excess La_2O_3 forming the $CuLa_2O_4$ phase (JCPDS # 96-153-1437) (Fig. S3) [57]. When the amount of La decreased to a La/Al molar ratio of 0.75 (La(0.75)AH2) (Fig. 1a), the La_2O_3 phase disappeared completely and the $LaAlO_3$ perovskite cubic phase became the main one, with a crystallinity index of 90 % (Table 3). This demonstrates that modifying the La content using the AH2 solution could induce the desired perovskite-type phase. Upon introducing Cu into the La(0.75)AH2 structure to form La(0.75)AH2-Cu, the XRD pattern (Fig. 1a) matched the theoretical perovskite pattern

Table 3
X-ray diffraction data and refinement parameters for $LaAlO_3$ perovskite.

Parameters	La(0.75) AH2	La(0.75)AH2-Cu	La(0.5)AH2-Cu
Crystal system	Cubic	Cubic	Cubic
Space group	Pm-3m	Pm-3m	Pm-3m
Crystallinity (%)[a]	90	89	79
Lattice parameters			
a = b = c (nm)	0.3802	0.3806	0.3797
α = β = γ (°)	90	90	90
Unit cell volume (nm^3)	0.05490	0.05513	0.05476
Bond distance			
La-O (nm)	0.26882	0.26913	0.26851
Al-O (nm)	0.19009	0.19030	0.18987
Cu-O (nm)	–	0.19030	0.18987
Microstructure			
Average crystalline size (nm)[b]	43	32	40
Refinement parameter			
X^2	1.35	1.16	1.10
GOF	1.2	1.1	1.1

[a] Crystallinity (%) was calculated from the ratio of the integrated area of all crystalline peaks to the total integrated area under the XRD peaks.
[b] Calculated using the Scherrer equation.

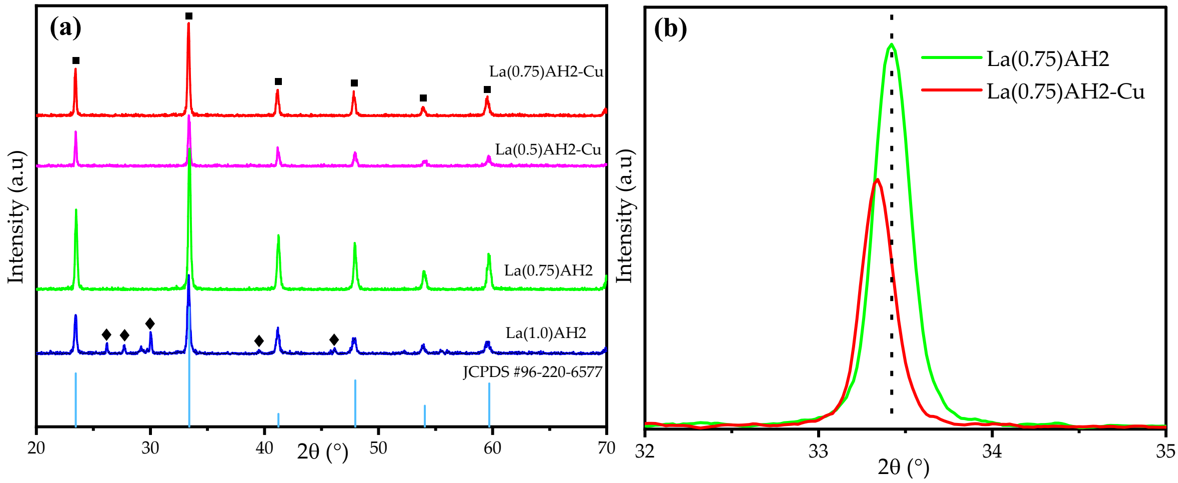

Fig. 1. (a) XRD patterns for $LaAlO_3$ perovskite prepared using AH2 with various La contents, and (b) magnified XRD patterns of La(0.75)AH2 and La(0.75)AH2-Cu. (■: $LaAlO_3$; (JCPDS # 96-220-6577); ◆: La_2O_3 (JCPDS # 96-101-0279)).

(JCPDS #96-220-6577), with no impurities being identified and a crystallinity index of 89 % (Table 3). This confirms the uptake of Cu into the perovskite structure despite the absence of CuO_x peaks. The low Cu loading and its good dispersion were consistent with this result. Compared to La(0.75)AH2, the (011) planes of the La(0.75)AH2-Cu catalyst exhibited a slight downshift in their 2θ value (from 33.42° to 33.34°). This shift, as shown in Fig. 1b, indicates the lattice relaxation due to Cu incorporation [58,59]. Additionally, La(0.75)AH2-Cu (32 nm) exhibited a smaller particle size compared to La(0.75)AH2 (43 nm) (Table 3). This decrease could be attributed to the incorporation of Cu, which may increase lattice distortion and suppress the growth of larger crystallites in the sample [60,61]. Similar changes in the crystallographic properties and microstructure were observed at a La/Al molar ratio of 0.5 (La(0.5)AH2-Cu) (Fig. 1a and Table 3). However, La(0.75)AH2-Cu showed stronger intensity in the XRD pattern (Fig. 1a), higher crystallinity (89 % vs. 79 %), and smaller particle size (32 vs. 40 nm) compared to La(0.5)AH2-Cu (Table 3). The lower La content in La(0.5)AH2-Cu could potentially lead to the formation of trace amounts of Al or Cu oxides, which may be undetectable by XRD. These undetected oxides, which were later identified by H_2-TPR, could potentially contribute to the lower crystallinity observed. According to previous reports [48,62], the percentage crystallinity is directly proportional to the amount of O species in the perovskite lattice.

The XRD patterns obtained for the materials were analyzed using the Rietveld method with the Fullproof Suite Toolbar [62–64]. The results of the Rietveld refinement for samples exhibiting the $LaAlO_3$ perovskite-like structure are included in Fig. 2. In these plots, observed values are shown with lines of various colors, calculated values as a solid black line with squares, and their difference as a blue line. Table 3 compares unit-cell parameters and other structural properties of La(0.75)AH2, La(0.75)AH2-Cu, and La(0.5)AH2-Cu. Compared to La(0.75)AH2, La(0.75)AH2-Cu exhibits an increase in the unit-cell volume (from 0.05490 to 0.05513 nm^3) and atomic distances (La–O: from 0.26882 to 0.26913 nm; Al–O: from 0.19009 to 0.19030 nm) that can be attributed to the larger ionic radius of Cu^{2+} (0.062 nm) compared to Al^{3+} (0.053

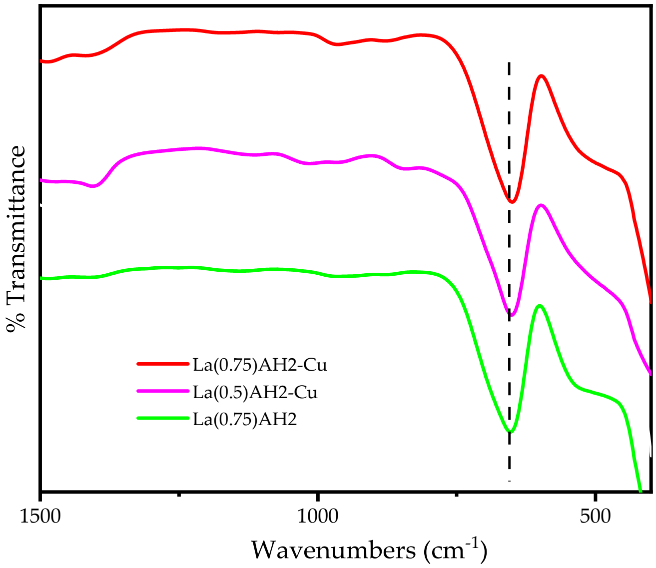

Fig. 3. ATR-IR spectra for La(0.75)AH2, La(0.75)AH2-Cu and La(0.5)AH2-Cu.

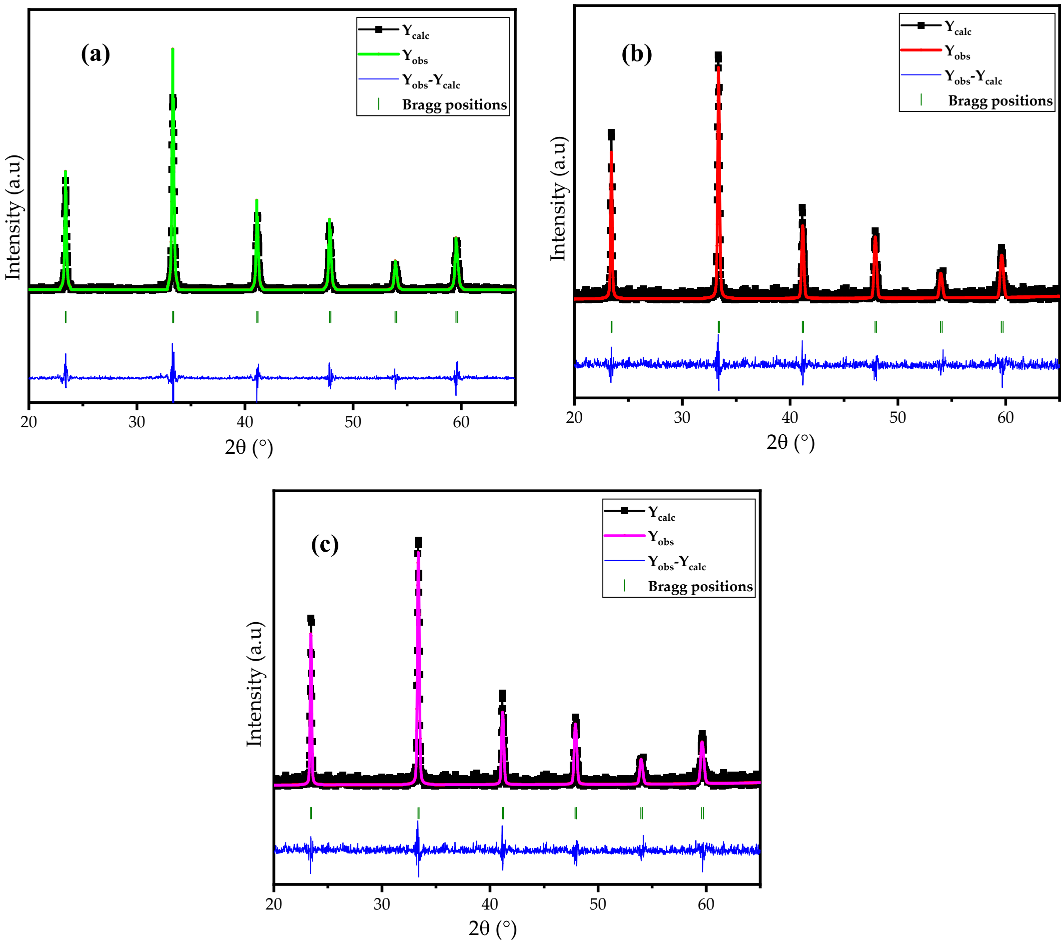

Fig. 2. Rietveld refinement plots of: (a) La(0.75)AH2; (b) La(0.75)AH2-Cu; (c) La(0.5)AH2-Cu.

nm) upon the cationic substitution of Al^{3+} with Cu^{2+}. The goodness-of-fit (GoF) index falls between 1.1 and 1.2, and the χ^2 (chi-squared) value ranges from 1.16 to 1.35 (Table 3), thus indicating a good fit for the structural model.

The observed slight shift of the ATR-IR signal to lower frequency (from 655.4 to approximately 645 cm^{-1}) in La(0.75)AH2-Cu and La(0.5)AH2-Cu compared to La(0.75)AH2 (Fig. 3) also supported the incorporation of Cu into the perovskite crystal lattice. The shift in the absorption band [65] suggests the incorporation of Cu into the octahedral AlO_6 structure characteristic of the perovskite lattice [34]. These results also indicate that the perovskite structure remained intact during the Cu-incorporation process. A similar behavior was observed when comparing La(1.0)AH2-Cu and La(1.0)AH2 (Fig. S4).

The TGA, DTG, and DTA curves for the precursor powders heat-treated at 200 °C for La(1.0)AH2-Cu-200 and La(0.75)AH2-Cu-200 are included in Fig. S5. The samples exhibited similar behavior in terms of the number of mass loss steps and the enthalpy of the reaction profile, with notable differences in percentage mass losses and the temperature difference in the thermal events. The TGA data revealed four mass-loss steps. The first step (I), which occurs between 30 and 313 °C, is due to the desorption of physisorbed water and the elimination of chemisorbed hydroxyl groups [62,66]. The second stage (II), extending up to approximately 403 °C, primarily involves the oxidation of residual organic compounds and the formation of oxycarbonate intermediates.

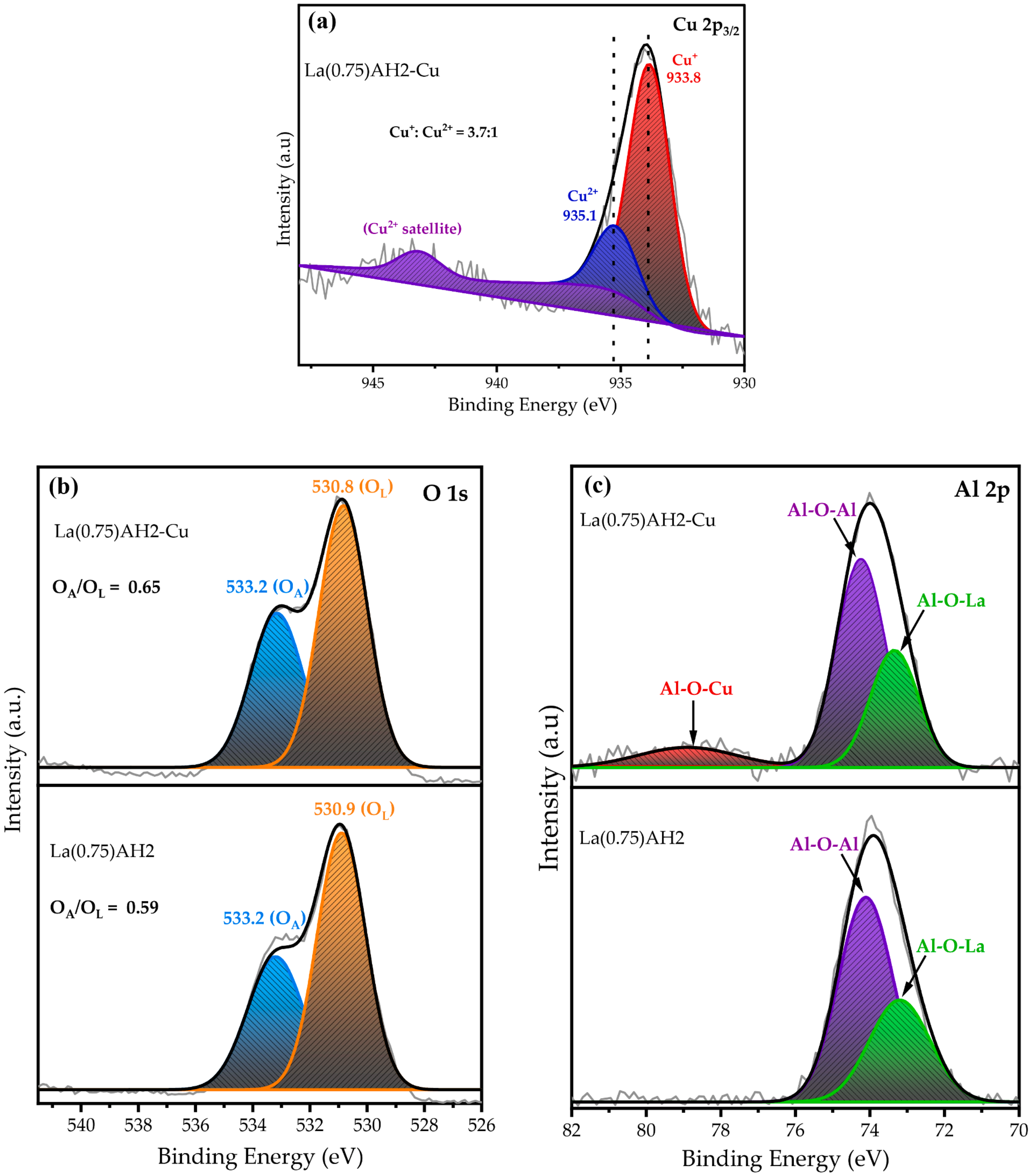

Fig. 4. (a) Cu $2p_{3/2}$ XPS spectra for La(0.75)AH2-Cu; (b) O 1s XPS spectra for La(0.75)AH2 and La(0.75)AH2-Cu; (c) Al 2p XPS spectra for La(0.75)AH2 and La(0.75)AH2-Cu.

The third event (III), up to around 546 °C, is attributed to the decomposition of residual nitroso groups from the La- and Cu-precursor salts, dissociation of the polymer network, and oxidation of organic carbon [67]. The sum of the mass losses in stages (II) and (III) indicates that the La(1.0)AH2-Cu-200 sample experienced a higher mass loss (57.54 %) than the La(0.75)AH2-Cu-200 material (33.81 %), which can be linked to the lower La/Al ratio used in the synthesis and thus lower content of nitroso groups from the La precursor. The exothermic events of stages (II) and (III) occurred at a lower temperature range (313–495 °C in La (0.75)AH2-Cu-200 compared to 362–546 °C in La(1.0)AH2-Cu-200), which might favor the subsequent crystallization step. Finally, the fourth step (IV), which occurred above 546 °C for La(1.0)AH2-Cu-200 and above 495 °C for La(0.75)AH2-Cu-200, is attributed to the decomposition of carbonate-type intermediates, leading to the formation of the perovskite [62,67], as earlier suggested by the XRD and ATR-IR analyses.

The surface elemental composition, oxidation states of the surface metal species, and chemical bonding of the materials were analyzed by XPS. The typical XPS survey spectra revealed the presence of the corresponding elements on the surface of La(0.75)AH2 and La(0.75)AH2-Cu powders (Fig. S6a). The presence of Cu was confirmed by detection of the Cu 2p peak in the La(0.75)AH2-Cu spectrum. Two prominent peaks are observed in the La 3d region, located at approximately 833 (La 3d$_{5/2}$) and 850 eV (La 3d$_{3/2}$), in Fig. S6a. These peaks correspond to La^{3+} and are present in both La(0.75)AH2 and La(0.75)AH2-Cu. Unlike other Cu-doped $LaAlO_3$ catalysts reported in the literature lacking La deficiency [10,34], the spin–orbit splitting signal of La 3d$_{5/2}$ and La 3d$_{3/2}$ did not exhibit a shift towards lower values compared to the undoped aluminate. Conversely, both binding energies increased by 0.2 eV and 0.4 eV, respectively, when comparing La(0.75)AH2 and La(0.75)AH2-Cu. This increase in the binding energy means an increase in the electric dipole moment and enhanced electron transfer [68], potentially reducing the energy barrier for electron diffusion from La to O and thereby with a potential benefit of the CWPO process.

In the Cu 2p$_{3/2}$ spectrum of La(0.75)AH2-Cu (Fig. 4a), the peak at ca. 935.1 eV, along with a shake-up satellite peak at 943.8 eV, corresponds to the presence of Cu^{2+} species [10,34,69]. The peak at ca. 933.8 eV corresponds to the reduced state of Cu species (i.e., Cu^{+}). These results indicate the coexistence of both Cu^{+} and Cu^{2+} on the catalyst surface, with a high Cu^{+}:Cu^{2+} atomic ratio of 3.7:1. This high proportion of Cu(I) compared to Cu(II) can be attributed to the deficiency of La, which regulates the average valence state of the Cu cations in the catalyst by creating an electron-rich center on the catalyst surface [36]. This finding is significant because a higher Cu^{+}/Cu^{2+} ratio in the octahedral lattice of the perovskite has been shown to correlate with enhanced catalytic performance and stability [34]. This is attributed to facilitation of the interfacial electron transfer cycle from Cu^{+} to Cu^{2+} upon reaction with H_2O_2, consequently promoting the generation of active species (HO•, HO$_2$•/$O_2^{\bullet-}$, etc). This means that the La(0.75)AH2-Cu catalyst, with its high Cu^{+}/Cu^{2+} ratio, exhibits a high electron density around the copper center, which can facilitate the reduction of H_2O_2. Cu^{+}, being highly reactive in the presence of hydrogen peroxide, can generate hydroxyl radicals (HO•), which are essential as potent oxidizing agents in the CWPO process. These radicals can efficiently degrade carbofuran and natural organic matter present in the reaction medium. The oxidized copper (Cu^{2+}) present in the catalyst, as well as that generated during the redox reaction, can be reduced back to Cu^{+} by reacting with intermediate organic compounds in the reaction medium [34]. Cu^{+} is predominantly formed on the catalyst surface, a process that can be facilitated by the presence of oxygen bridges between neighboring copper ions. These oxygen bridges can support the transfer of electrons necessary for reducing Cu^{2+} to Cu^{+} and stabilize the reduced copper state [41]. This mechanism can enhance the efficiency of the catalyst and reinforce its durability across multiple reaction cycles. Furthermore, Li *et al.* [70] have recently demonstrated that Cu^{2+} on the catalyst surface can also activate H_2O_2 and generate additional reactive oxygen species, such as HO$_2$•, which can further contribute to contaminant degradation.

The O 1 s XPS spectra of La(0.75)AH2 and La(0.75)AH2-Cu (Fig. 4b) exhibited two peaks. The first peak, O$_L$, appears at 530.9 and 530.8 eV for La(0.75)AH2 and La(0.75)AH2-Cu, respectively, and is attributed to lattice O (La–O, Al–O, and Cu–O). The second peak, O$_A$, appears at 533.2 eV and corresponds to adsorbed O (primarily O vacancies (V$_O$) formed by physically and chemically adsorbed water, hydroxyl groups, point defects on the lattice, line defects, and surface defects [60,71,72]. The ratios of adsorbed O (O$_A$) to lattice O (O$_L$) for La(0.75)AH2 and La (0.75)AH2-Cu were 0.59 and 0.65, respectively (Fig. 4b). It is suggested that Cu^{2+}, which has a larger ion radius, may replace Al^{3+}, with a smaller ion radius, thus leading to distortion of the perovskite structure, an increase in the concentration of O vacancies, increasing the ratio of O$_A$ to O$_L$. According to a previous study [10], V$_O$ increased by 28 mol% with the incorporation of Cu. The substitution of Al (with oxidation state of 3+) by Cu ions (with an oxidation states of 2+ or 1+) in the perovskite structure induces a local charge imbalance within the material. Therefore, to maintain charge neutrality, oxygen vacancies (adsorbed oxygen) are formed by releasing lattice oxygen. The higher positive charge of the Al^{3+} ion compared to the Cu ions promotes this compensation within the crystal structure based on the principle of electrical neutrality [73,74]. Additionally, the deficiency or vacancies of La (V$_{La}$) in the perovskite structure can also contribute to the creation of O vacancies on the catalyst's surface [36]. For this reason, the perovskite without Cu ((La0.75) AH2) exhibited a higher content of O vacancies (O_A/O_L=0.59), as observed in Fig. 4. This differs from the $LaAlO_3$ perovskite reported in the literature [48,64,75], which has an La/Al molar ratio 1:1 and has shown less O vacancies (O_A/O_L<0.40) using a similar synthetic method. Therefore, the La(0.75)AH2-Cu catalyst includes a contribution from these O species coming from La(0.75)AH2. Chemisorbed O species are known to be more reactive than lattice O [76], which suggests that the high concentration of surface V$_O$ in La(0.75)AH2-Cu could promote H_2O_2 activation in the heterogeneous Fenton/Fenton-like system [36,77], since in solid materials, O vacancies often contain unpaired electrons, which may participate in the catalytic process [78]. The high-resolution Al 2p spectra of La(0.75)AH2 and La(0.75)AH2-Cu, around 74 eV (see Fig. 4c) fitted well with two peaks corresponding to the Al–O–Al and Al–O–La bonds in the perovskite-type $LaAlO_3$ [10,62,79]. An additional peak at a binding energy of 78.7 eV in La(0.75)AH2-Cu was assigned to the Al–O–Cu bond [34,80]. According to previous reports [10,81], this peak corresponds to Cu 3p$_{1/2}$ in Cu^{+}. This means that partial charge delocalization can occur between aluminum and copper in the Al-O-Cu bond due to their different electronegativities. Copper's higher electronegativity can lead to a redistribution of electron density towards itself. This can result in a partial positive charge on aluminum and a partial negative charge on copper. This result further confirms the isomorphic substitution of Al by Cu within the perovskite lattice, maintaining both the structural integrity and charge balance of the material. The SEM image of the La(0.75)AH2 perovskite (Fig. 5a) showed the typical sphere-like morphology of $LaAlO_3$ perovskites, with high agglomeration and a smooth, crack-free surface [35,82]. In contrast, after incorporation of Cu (La(0.75)AH2-Cu; Fig. 5b), the particles exhibited increased dispersion and a rougher surface with protrusions. In addition, the crystal particles appeared more mature, displaying a fluffy cotton-like morphology. To investigate the elemental distribution of these materials, 3D SEM images with color contrast (Fig. 5a and 5c) were acquired, along with energy-dispersive spectroscopy (EDS) (Fig. 5b) and SEM elemental mapping analysis (Fig. 5d). The EDS spectrum confirmed the presence of La, Al, O, and Cu in La(0.75) AH2 and La(0.75)AH2-Cu. The elemental mapping of La(0.75)AH2-Cu confirmed a uniform distribution of all elements on the surface of the catalyst. The 3D SEM images (Fig. 5a and 5c) further demonstrate the uniform distribution of Cu active sites in the La(0.75)AH2-Cu catalyst and the presence of some Cu aggregates in the La(0.75)AH2 starting material derived from W.

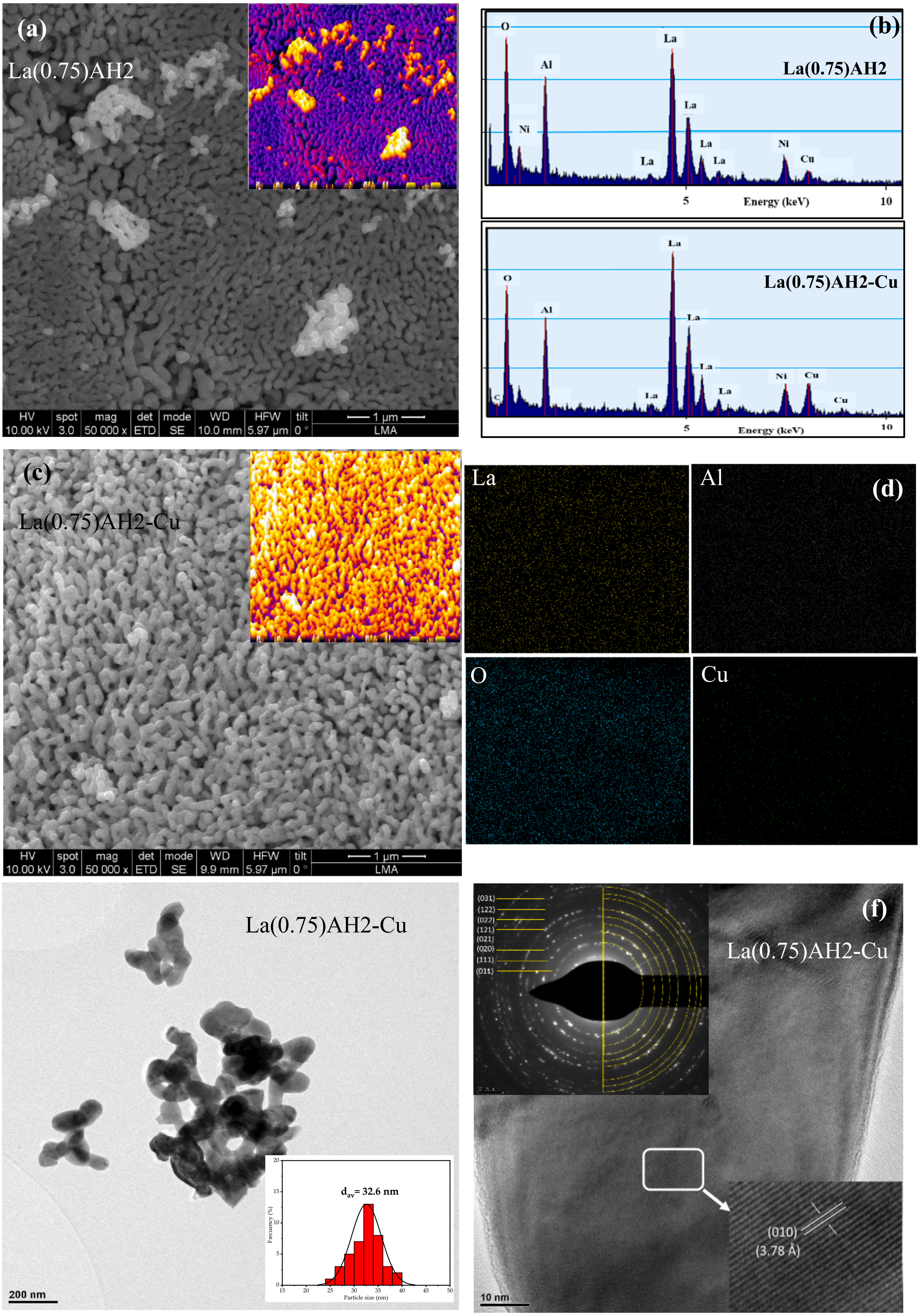

Fig. 5. 2D/3D SEM image (a) of La(0.75)AH2, EDS (b) of La(0.75)AH2 and La(0.75)AH2-Cu. 2D/3D SEM image (c), elemental mapping (d) TEM image and particle-size distribution (e), and HRTEM with SAED image (f) of La(0.75)AH2-Cu.

The XRF results for the materials prepared are summarized in Table S2. The measured La:Al:Cu molar ratio in the La(0.75)AH2-Cu catalyst was 0.78:0.94:0.06, which is similar to the expected molar ratio for the $La_{0.75}Al_{0.95}Cu_{0.05}O_{3-\delta}$ sample. The combination of the XRF (Table S2) and XRD (Fig. 1a) results for the La(1.0)AH2 material confirms that all Al atoms from AH2 combine with La to form the $LaAlO_3$ perovskite phase, while the remaining La atoms formed the La_2O_3 phase. Therefore, it is necessary to decrease the content of La atoms added to an La/Al molar ratio of 0.75 (La(0.75)AH2) or 0.5 (La(0.5)AH2-Cu) to promote the pure $LaAlO_3$ perovskite phase. Both materials displayed La:Al:Cu molar ratios of 0.85:0.98:0.02 and 0.52:0.93:0.07, respectively (Table S2). Trace amounts of Cu were identified in both materials, originating from the starting saline slag (W) (Table S3) and specifically extracted during the second acid treatment. These results are consistent with the previously discussed EDS and SEM results.

The TEM image of La(0.75)AH2-Cu (Fig. 5e) revealed spherical nanoparticles with a low agglomeration state. These nanoparticles have a diameter of 32.6 nm, consistent with the values estimated by XRD using the Scherrer equation, thus confirming their small size. In contrast, the TEM image of La(0.75)AH2 (Fig. S7a) showed highly agglomerated nanoparticles with a larger diameter of 40.6 nm. The HRTEM image (Fig. 5f) revealed a lattice spacing of 0.378 nm, corresponding to the (0 1 0) planes of the cubic phase of perovskite (JCPDS #96-220-6577) in La(0.75)AH2-Cu. The HRTEM image of La(0.75)AH2 (Fig. S7b) exhibits a lattice spacing of 0.374 nm for the same plane. These results corroborate perovskite formation and the successful incorporation of Cu into the perovskite framework, also confirmed the lattice relaxation and that the lattice structure was not destroyed during the Cu-incorporation process. The absence of CuO lattice fringes in the HRTEM images suggests that the Cu-incorporation process did not introduce other Cu oxide phases besides the perovskite phase [58]. The selected-area electron diffraction (SAED) patterns of La(0.75)AH2 and La(0.75)AH2-Cu (Fig. 5f and Fig. S7b, respectively) exhibited discrete diffraction rings, which can be indexed to the (0 1 1), (1 1 1), (020), (021), (121), (022), (122), and (031) crystal planes of the $LaAlO_3$ phase. This confirms the good crystallinity and lattice integrity of the synthesized perovskites, and, therefore, the perovskite nature of the materials [58].

La(1.0)AH2, La(1.0)AH2-Cu, La(0.75)AH2 and La(0.75)AH2-Cu exhibit type II isotherms in N_2 adsorption measurements (Fig. S8) [34,48,60]. The nearly linear behavior at low relative pressure (p/p^0) suggests unrestricted monolayer or multilayer adsorption, further indicating the presence of macropores [83,84]. As the relative pressure (p/p^0) decreased, both samples displayed an H3 hysteresis loop ($0.4 < p/p^0 < 0.99$) characteristic of mesopores [83,85]. This hysteresis loop typically arises from capillary condensation within the pores [85,86]. Specifically, the H3-type loop suggests slit-shaped pores or disordered plate-like structures [85,87]. This type of loop exhibited a narrow shape with steadily rising slopes in both adsorption and desorption curves as the pressure increases, thus indicating a rapid increase in adsorbed N_2. Notably, H3-type hysteresis loops are often associated with the development of pores in aggregated perovskite composites [85].

The S_{BET} surface areas of La(0.75)AH2 and La(0.75)AH2-Cu were 11 $m^2\ g^{-1}$ (Table S6). Low BET surface areas are common in perovskites due to the high calcination temperature used during sample preparation [80]. However, the total pore volume of La(0.75)AH2-Cu (0.032 mL g^{-1}) was higher than La(0.75)AH2 (0.028 mL g^{-1}). This increase can be attributed to the successful incorporation of Cu into La(0.75)AH2, potentially creating new active sites for H_2O_2 activation. In contrast, when comparing La(1.0)AH2 with La(1.0)AH2-Cu, a decrease in both the S_{BET} (from 13 to 7 $m^2\ g^{-1}$) and the total pore volume (from 0.035 to 0.021 mL g^{-1}) was observed. This decrease is likely due to formation of the extra-framework La_2CuO_4 phase in the La(1.0)AH2-Cu catalyst, which apparently blocked pores of the material. In addition, La_2CuO_4 exhibits a tetragonal spinel crystal structure, which has a lower packing density than the cubic perovskite crystal structure. Consequently, when both structures coexist, they can generate defects and interfaces in the material, which reduces the specific surface area. The La(0.5)AH2-Cu material also exhibits a low specific surface area (8 m^2/g) and a low total pore volume (0.013 mL g^{-1}) compared to La(0.75)AH2-Cu (Table S6). This is due to the formation of Al and Cu oxides that can block the porosity of the material. These results are consistent with those obtained using XRD and XRF techniques.

The H_2-TPR profiles of all the catalysts prepared are shown in Fig. S9. The profile of La(0.75)AH2-Cu showed two primary H_2 consumption regions. The first region exhibits a prominent peak at around 363 °C. This temperature is significantly higher than the one reported in the literature for Cu reduction in perovskites also containing La and Al (290 °C) [58,88], but slightly higher than that showed by La(1.0)AH2-Cu (322 °C). This suggests a stronger bonding of Cu to the perovskite lattice in La(0.75)AH2-Cu, which confirms the possible absence of extra-framework CuO_x. In contrast, the low La content in La(0.5)AH2-Cu could promote formation of these oxides, which are mainly reduced at the lowest temperature (322 °C; Fig. S9). This behavior is not favorable for reducing metal leaching during CWPO catalysis, these results are consistent with all previous analytic techniques. The hydrogen consumption below 450 °C observed for La(0.75)AH2-Cu (with two deconvolutions to separate the overlapping signals between 415 °C and 450 °C) and below 414 °C observed for La(1.0)AH2-Cu (with two deconvolutions to separate overlapping signals between 389 and 441 °C), as well as the consumption below 385 °C for La(0.5)AH2-Cu, can be attributed to two concurrent processes: *(i)* the reduction of O chemisorbed on the catalyst surface and *(ii)* the progressive reduction of Cu^{2+} to Cu^+ throughout the perovskite lattice. This reduction maintains the electroneutrality and structural integrity of the perovskite [88,89]. In contrast, the H_2 consumption observed at a higher temperature ($TP_m > 500$ °C) for all catalysts (Fig. S9) is attributed to the reduction of Cu^+ to Cu^0. This reduction, like the previous one, starts at the surface and then grows towards the bulk of the material [88].

The total reduction rate of Cu species and the peak areas of the H_2-TPR curves have been calculated, as shown in Table S7. According to these results, it is evident that the La(0.5)AH2-Cu material exhibited the highest reduction (66 %) at the lowest temperature ($TP_m = 322$ °C), with a well-defined peak. This reduction is approximately double that observed for the La(0.75)AH2-Cu (31 % at $TP_m = 363$ °C) and La(1.0)AH2-Cu (35 % at $TP_m = 331$ °C) materials. This significant reduction is likely associated with the higher content of extra-framework CuO_x present in this material. Such copper species undergo weak electronic interactions with the perovskite, being more easily reducible [90]. The lower La content in this catalyst could potentially result in the formation of copper and aluminum oxides. Moreover, due to excess Al, Cu-Al spinel oxides may have formed. It is noteworthy that a recent study by Thongratkaew *et al.* [91], using H_2-TPR and H_2-TPD techniques, demonstrated that $CuAl_2O_4$ spinel exhibited a high capacity for H_2 absorption at relatively low temperatures, indicating that atomic hydrogen species could be incorporated into the spinel structure. Note that, due to its low quantity, this phase could not be clearly detected by XRD, as it was likely below the detection limit of this technique. This suggests that in the La(0.5)AH2-Cu material, the high hydrogen consumption at lower temperatures can be associated with the Cu oxides being more exposed to H_2, resulting in a nearly single-stage reduction of Cu^{2+} to Cu^+, and possibly also with the absorption of H_2 by the formed spinel. In contrast, the La(0.75)AH2-Cu ($TP_m = 415$ and 450 °C) and La(1.0)AH2-Cu ($TP_m = 389$ and 414 °C) catalysts displayed two additional reduction stages, with similar reduction percentages in both stages, showing total values of 48 % and 46 %, respectively. These values are higher than those of the La(0.5)AH2-Cu catalyst ($TP_m = 385$ °C), which exhibited a 24 % reduction. This suggests that the first two catalysts experienced a more gradual reduction of Cu^{2+} to Cu^+, likely due to the strong bonding of octahedral copper within the perovskite structural framework and its progressive reduction across the perovskite lattice.

The reduction percentages at $TP_m > 500$ °C, attributed to the reduction of Cu^+ to Cu^0, were 21 % for the La(0.75)AH2-Cu catalyst

($TP_m = 616\ ^\circ C$) and 18 % for the La(1.0)AH2-Cu catalyst ($TP_m = 554\ ^\circ C$) (Table S7). These values are approximately double the reduction observed for the La(0.5)AH2-Cu catalyst (TP_m = 556 °C and 599 °C), which was 10 %. This confirms the higher reducibility of copper oxides in La(0.5)AH2-Cu at lower temperature. Finally, as mentioned earlier, the main differences in the reduction profiles between La(0.75)AH2-Cu and La(1.0)AH2-Cu are attributed to the shift to higher reduction temperatures in the case of the first. It is important to note, based on XRD results, that the La(1.0)AH2-Cu material contains not only the perovskite phase but also the La_2CuO_4 phase. This suggests that, although the perovskite phase is typically robust, in this case, the interaction with the La_2CuO_4 phase seems to result in reduced stability of the Cu incorporated into the perovskite crystal lattice [92]. Furthermore, this phase may provide additional reduction sites or alter the stable electronic distribution of Cu within the structure.

3.2. Statistical optimization of the catalytic CBF removal

The complete results of the statistical design of experiments (DOE) are summarized in Table 4. This dataset was analyzed using the response surface methodology (RSM) to maximize all responses and minimize Cu leaching, as shown in Fig. 6 (a–e). The single-response quadratic statistical models developed are summarized in Eqs. (4)–(7). These models consider the following factors: (A) catalyst concentration (mg Cu/mg H_2O_2); (B) H_2O_2 dosage; and (C) pH.

$$\begin{aligned} Degradation(\%) = {} & 24.0757 - 426.5A - 0.22842B + 18.8795C \\ & + 656.635A^2 + 5.64073AB - 7.28528AC \\ & + 0.000763523B^2 - 0.0830938BC - 0.922177C^2 \end{aligned} \tag{4}$$

$$\begin{aligned} Mineralization(\%) = {} & 78.9033 + 225.203A - 0.0350332B - 11.4272C \\ & + 527.385A^2 - 0.376914AB - 55.3101AC \\ & + 0.00129209B^2 - 0.0425BC + 1.2424C^2 \end{aligned} \tag{5}$$

$$\begin{aligned} H_2O_2Reacted(\%) = {} & 66.4433 - 67.5848A + 0.0574912B - 4.21224C \\ & + 100.374A^2 + 1.28253AB + 17.2637AC \\ & - 0.00438173B^2 + 0.103844BC - 0.33076C^2 \end{aligned} \tag{6}$$

$$\begin{aligned} CuLeached\left(mgL^{-1}\right) = {} & -1.96856 + 10.0286A + 0.0460988B \\ & + 0.47311C - 13.0912A^2 + 0.785041AB \\ & - 8.38897AC + 0.000391125B^2 - 0.0308437BC \\ & + 0.171658C^2 \end{aligned} \tag{7}$$

The individual response models exhibited a good fit, with correlation coefficients (R^2) between 0.60 and 0.86. Subsequently, simultaneous optimization of all targeted responses (Fig. 6e) was achieved using these models as input, resulting in a highly desirable outcome with a value of 0.940 out of a possible 1.0 at the optimum condition.

The analysis of variance did not show statistical significance for the CBF degradation response (Fig. 7a). However, the La(0.75)AH2-Cu catalyst, used in the CWPO process, achieved high pesticide-degradation rates in NOM, reaching up to 85.5 % in experimental trial 9 (Table 4). This result was obtained at near-neutral pH after 180 min of reaction, using the low experimental levels (–1) of catalyst concentration and peroxide dosage. Keeping proper catalytic response at near-neutral conditions can be of pivotal interest in the real-scale agricultural wastewater treatment, since the pH of these effluents is reported to be higher than 6.2 [45,46]. These results agree with other studies

Table 4

Experimental results of DOE catalytic tests, optimum, control, and catalyst reuse experiments.

Run	Factors			Responses			
	Catalyst Concentration (mg Cu/mg H_2O_2)	H_2O_2 Dosage	pH	Degradation (%)	COD Mineralization (%)	H_2O_2 Consumed (%)	Cu Leached (mg L^{-1})
1	0.119	26.4	5.0	25.3	44.7	51.0	1.34
2	0.119	93.6	5.0	60.4	41.1	70.1	1.39
3	0.119	60.0	1.6	16.0	76.2	51.4	5.33
4	0.119	60.0	5.0	26.9	44.6	41.0	1.39
5	0.119	60.0	5.0	61.3	37.3	70.6	0.96
6	0.119	60.0	5.0	84.1	26.2	82.6	1.06
7	0.119	60.0	5.0	53.5	40.2	66.9	1.34
8	0.187	40.0	3.0	53.9	79.6	73.0	1.15
9	0.050	40.0	7.0	85.5	34.3	44.6	0.97
10	0.119	60.0	5.0	53.3	43.9	70.9	1.39
11	0.119	60.0	5.0	47.6	46.6	77.5	1.34
12	0.234	60.0	5.0	55.6	51.9	76.1	1.34
13	0.187	80.0	7.0	73.5	16.9	83.5	0.70
14	0.050	80.0	7.0	50.6	31.5	63.9	0.97
15	0.003	60.0	5.0	46.0	45.0	57.4	0.15
16	0.119	60.0	8.4	47.1	35.4	72.0	0.50
17	0.119	60.0	5.0	52.9	35.5	72.7	1.34
18	0.050	80.0	3.0	48.4	50.9	55.1	1.15
19	0.119	60.0	5.0	55.2	44.6	64.8	0.96
20	0.119	60.0	5.0	55.0	52.7	72.9	1.39
21	0.187	80.0	3.0	63.0	81.5	82.8	10.40
22	0.050	40.0	3.0	57.7	61.7	69.8	1.14
23	0.187	26.4	7.0	65.3	36.6	74.6	1.31
Optimum (mod)	0.234	73.3	6.2	77.6	36.0	92.2	1.97
Optimum (exp)	0.234	73.3	6.2	94.1	41.7	71.2	0.83
Hydrogen peroxide	0.000	73.3	6.2	26.0	12.2	37.0	NA
Catalyst adsorption	0.234	0.0	6.2	30.6	13.9	NA	0.12
Reuse 1	0.234	73.3	6.2	86.5	36.0	70.1	1.20
Reuse 2	0.234	73.3	6.2	80.1	32.4	69.4	1.30
La(1.0)AH2-Cu	0.234	73.3	6.2	79.4	32.5	50.0	1.03

NA: Not applicable.

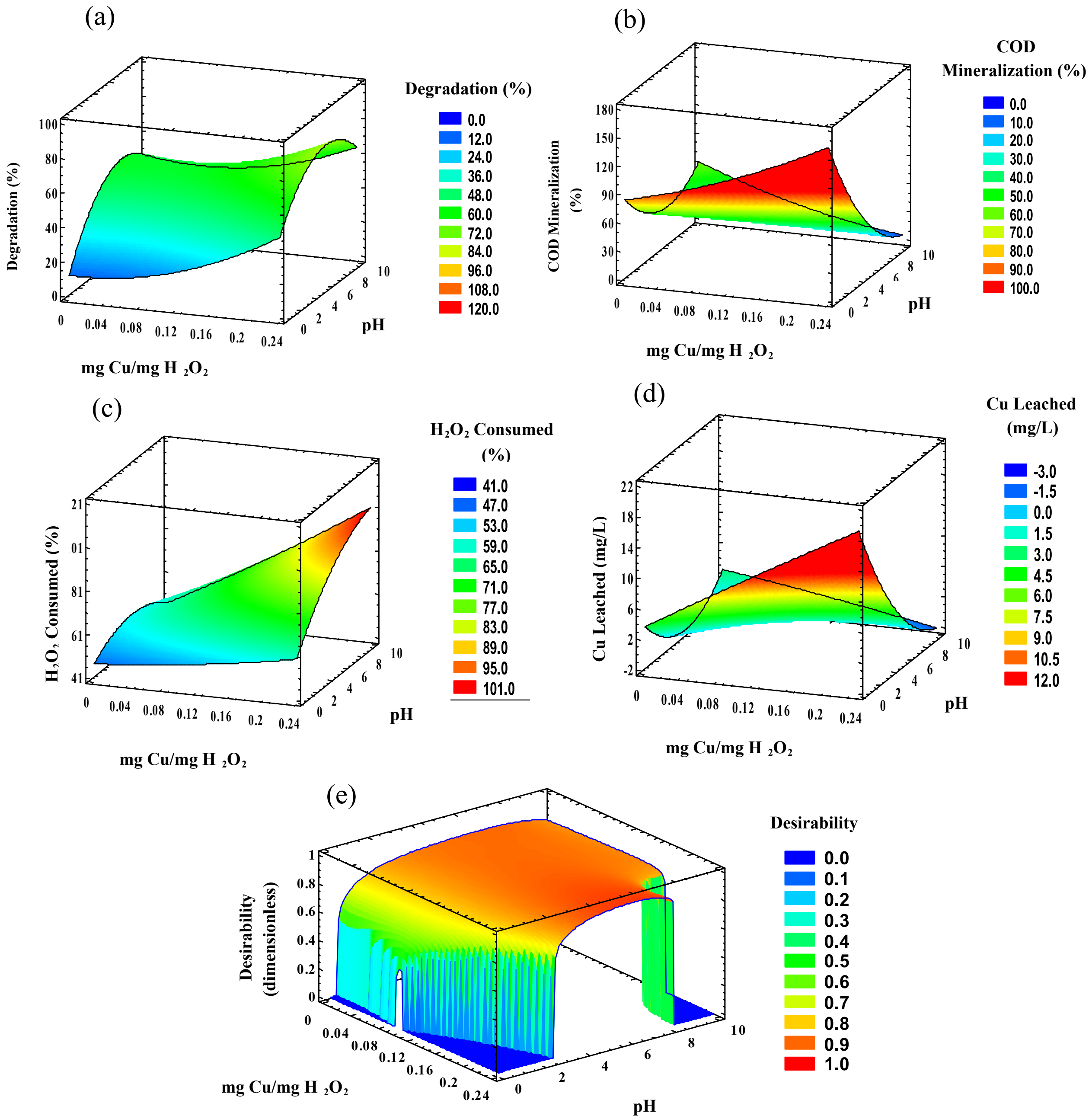

Fig. 6. Estimated response surface plots for DOE set of experiments: (a) CBF degradation; (b) COD mineralization; (c) hydrogen peroxide consumed; (d) Cu leached; and (e) multi-response surface based on desirability function.

[10,34,57] that have demonstrated high catalytic activity in the degradation of various refractory compounds at a pH close to 7.0 for perovskite-type catalysts with Cu active sites. These studies employed electron paramagnetic resonance (EPR) with a DMPO spin trap to detect reactive O species (ROS) and have shown that hydroxyl radicals (HO•) are the primary oxidizing species formed. This occurs due to the reduction of H_2O_2 on the surface of the perovskite-type catalyst. Hydrogen peroxide can accept electrons from the Cu center in the catalyst, facilitated as shown before by the significant presence of Cu^+, this is evidenced in the Cu $2p_{3/2}$ XPS spectrum for La(0.75)AH2-Cu (Fig. 4a). Additionally, some organic intermediates can further enhance the degradation process by acting as electron donors [34], promoting the reduction of H_2O_2 on the catalyst surface, eventually leading to the efficient overall degradation of the organic pollutants. As shown previously, a higher electron density around the Cu center and a greater abundance of octahedral Cu^+ sites (due to its cationic substitution by Al^{3+} and the deficiency of La) can contribute to the effective reduction of H_2O_2 into hydroxyl radicals (HO•). These electron-donating contaminants can also interact with surface Cu atoms, thereby facilitating the Cu(II)/Cu(I) redox cycle, whereas weakening the O–O bond of H_2O_2 on the catalyst surface.

The Pareto's diagram for COD mineralization (Fig. 7b) showed an inverse relationship with pH; in other words, lower pH values favored the mineralization of CBF and NOM in the reaction medium. Such an effect is well known in general for Fenton-like processes, since the reduction potential of the ROS decreases as the pH increases, however, it can be also influenced in this case by the homogeneous Fenton process, since the Cu leaching showed also to be significantly favored at lower pH values, as observed in Fig. 7d. Thus, lowering of Cu leaching exhibited a high negative statistical significance with respect to pH. Interactions BC

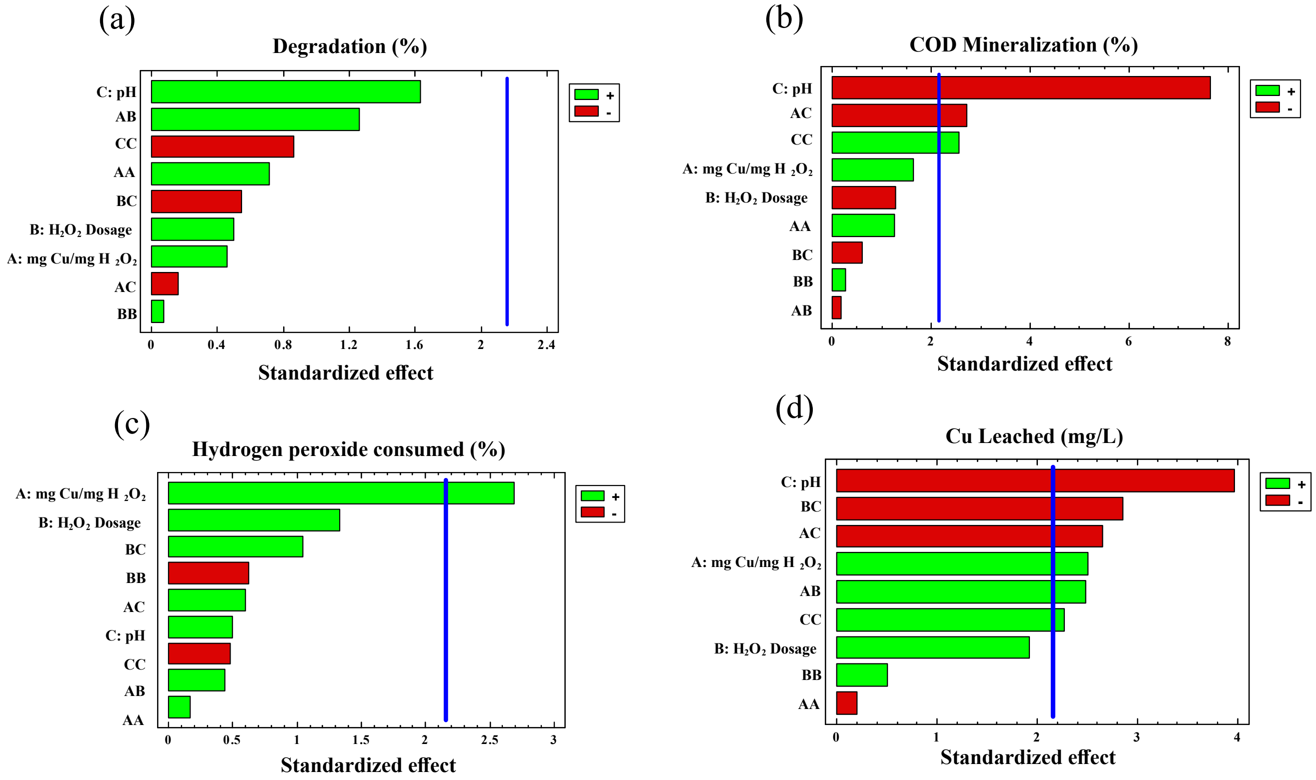

Fig. 7. Pareto charts of standardized effects from the design of experiments (DOE) for CBF degradation, COD mineralization, hydrogen peroxide consumed, and Cu leached.

and AC showed negative statistical significance, hence implying that the combination of H_2O_2 dosage and pH, as well as the interaction between catalyst concentration and pH, jointly influenced the desired response, mainly driven by the pH effect just mentioned. In contrast, variables A (catalyst concentration) and AB (interaction between catalyst concentration and H_2O_2 dosage) showed statistically positive effects on the same response. This implies that increasing the catalyst concentration and the interaction of catalyst concentration with H_2O_2 dosage has positive effects on minimizing leached Cu. This result may be due to the alkaline properties of the catalyst [35,93], which can increase the pH when dissolved in the reaction medium. All of the above indicates that adjusting and controlling pH levels can be crucial for optimizing the efficiency of the CBF mineralization process, along with CBF degradation, thus keeping the pH as close to neutrality as possible. Finally, analysis of the Pareto diagram for hydrogen peroxide consumption (Fig. 7c) reveals a positive statistical significance with respect to the catalyst concentration. This suggests an increased consumption of hydrogen peroxide as the amount of catalyst increases. This phenomenon can be mainly attributed to the higher presence of active Cu sites, which favor the reaction of H_2O_2 for the formation of HO•-type oxidizing species, as discussed previously.

The optimal conditions found according to the statistical analysis of the experimental data were: catalyst concentration (mg Cu/mg H_2O_2) = 0.234; H_2O_2 dosage = 73.3 % (i.e., 0.73-times the stoichiometric dose required for the COD full mineralization); and a pH of 6.2. It is remarkable for this catalytic system that the optimal pH is very close to the near-neutral pH featuring most agricultural wastewaters, which at the same time favors CBF degradation while minimizing the leaching of active sites from the catalyst. Furthermore, the optimal catalyst concentration enables a high utilization of H_2O_2 by the active Cu sites, leading, in turn, to the most efficient generation of highly oxidizing species like including hydroxyl radicals (HO•). These radicals attack organic substrates directly, thereby ultimately improving the overall efficiency of the CWPO process.

3.3. CBF degradation in the La(0.75)AH2-Cu activated CWPO process under optimized reaction conditions

Experiments conducted under optimal conditions for CBF degradation ("Optimum (exp)", Table 4) achieved 94.1 % CBF degradation, 41.7 % COD mineralization, 71.2 % hydrogen peroxide consumption, and 0.83 mg L^{-1} of leached Cu at 25 °C after 180 min of reaction, from a starting COD concentration of 22.8 mg L^{-1}. These results were also compared to two control experiments (Fig. 8a). Fouad *et al.* [54] reported that a dual perovskite-type photocatalyst (Ti-$LaFeO_3$) was used for the photo-Fenton degradation of 7.0 mg L^{-1} of CBF in the presence of 0.7 g L^{-1} of catalyst, a H_2O_2 dose of 480 mg L^{-1}, a pH of 3.0, and with an ultraviolet light lamp. These authors reported 90.6 % removal of the agrochemical and 52.3 % COD/TOC mineralization. However, this method required a dose of H_2O_2 almost 20 times higher than the optimum reported in this study, alongside the clearly acid pH. In addition, the CBF was dissolved in ultrapure water, whose conditions do not account for possible matriz effects preventing either degradation or carbon mineralization of the pesticide in natural conditions, finally, an external source of UV-radiation was required. Similarly, Samy *et al.* [94] evaluated the photocatalytic degradation of CBF in various water matrices (distilled, lake, tap, drainage, and seawater) using a (Ti:Ni) mixed-MOF catalyst. They observed a reduction in CBF degradation in each matrix compared to distilled water, with the greatest reduction (up to 33 %) occurring in seawater. The authors attributed that decrease to the presence of dissolved organic and inorganic compounds, as well as turbidity, in the water matrices. Therefore, the La(0.75)AH2-Cu catalyst reported in this study demonstrated outstanding CBF degradation and COD mineralization, even in NOM-doped water by the CWPO process and close to neutral pH. This is attributed to the fact that the reduction of H_2O_2 to HO• was promoted by the cycle of high and low electron density around the Cu center in the catalyst, which is not that sensitive to the solution pH. This results in a wide pH application range and high efficiency, even at near-neutral pH, without the need for external radiation

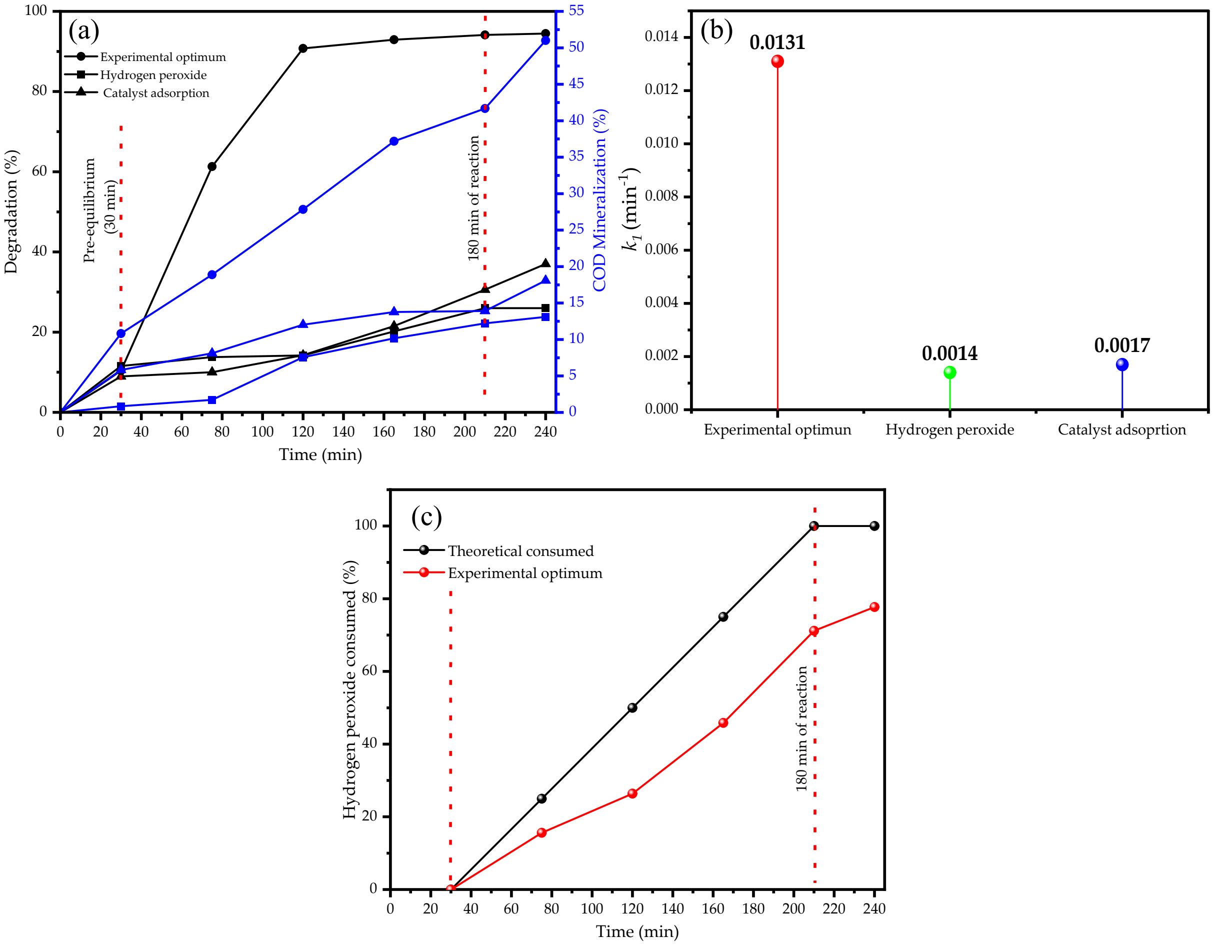

Fig. 8. (a) Performance of CWPO degradation and mineralization of CBF under multi-response optimal conditions using La(0.75)AH2-Cu as catalyst. Several control experiments are included for comparison, such as the effect of catalyst adsorption and direct hydrogen peroxide attack. (b) The pseudo first-order reaction rate constant. (c) Hydrogen peroxide consumed vs. reaction time. Curves for theoretical consumption and under optimal reaction condition are shown. Catalyst concentration (mg Cu/mg H_2O_2) = 0.234, H_2O_2 dosage = 73.3 %, pH 6.2, $[TOC]_0$ = 22.8 mg C·L^{-1}, T=25 °C.

Table 5
Comparative study of CBF removal.

Catalyst	CBF concentration (mg/L)	Catalyst dose (g/L)	pH	H_2O_2 dose (%)*	Degradation (%)	Ref.
La(0.75)AH2-Cu	3.0	2.0	6.2	73.3	94.1	this study
FeNT	3.3	0.5	3.5	> 100	76.0	[4]
Ti–$LaFeO_3$	7.0	0.7	3.0	> 100	90.6	[54]
Fe_3O_4-SnO_2-gC_3N_4	0.1	3.5×10^{-3}	6.0	NA	88.9	[103]
WO_3	20	1.0	7.0	NA	88.0	[104]
$NaNbO_3$–Au–Sn_3O_4	0.1	0.4	NR	NA	73.0	[105]
TiO_2	17.7	1.4	7.0	NA	92.8	[106]
TiO_2	0.1	0.3	8.4	NA	82.0	[107]
NM/ZnO/AC	5.0	0.5	7.0	NA	67.2	[1]
MIL-125(Ti)	10.0	0.5	7.0	NA	40.1	[94]
(Ti:Ni) MMOF	10.0	0.5	7.0	NA	82.2	[94]
(2Ti:Ni) MMOF	10.0	0.5	7.0	NA	69.4	[94]

* Percentage of stoichiometric H_2O_2 dosage for COD oxidation.
NA: Not applicable.
NR: Not reported.

sources. Additionally, by substituting Cu with Al in the perovskite lattice and with the presence of La vacancies, oxygen vacancies were generated in the catalyst. These vacancies act as 'Fenton-catalytic' centers, facilitating the dissociation of H_2O_2 and the generation of HO• through a surface confinement pathway [77]. Therefore, at near-neutral pH, there was likely a synergistic effect in the generation of hydroxyl radicals, due to the efficient redox cycle of Cu located in the octahedral sites of the perovskite and the contribution of the OVs.

The catalyst here studied utilizes an active metal undergoing rather low leaching (0.83 mg L^{-1}, Table 4), which is consistent with the H_2-TPR results discussed earlier. Moreover, this result indicates that the Cu^{2+} ions released were not predominant in CBF degradation. According to US regulations, the maximum Cu limit in drinking water is 1.3 mg L^{-1}, and EU directives establish a limit of 2.0 mg L^{-1} [10,95]. As such, the release of 0.83 mg L^{-1} Cu^{2+} do not exceed even the acceptable range for drinking water. Futhermore, the high efficiency of the degradation process in this study was achieved at a pH close to neutrality, thereby simulating real wastewater conditions and resulting in a significant discoloration of the polluted water after the CWPO reaction (Fig. S2). The brown color of the water mainly originates from the humic acids (HA) present in the synthetic NOM standard solution, but also in common surface water sources (lakes, rivers, etc) (Table S1). A comparison of the performance of the La(0.75)AH2-Cu catalyst prepared in this study in the degradation of CBF with respect to other catalysts reported in the literature can be found in Table 5. For example, the La(0.75)AH2-Cu catalyst in the CWPO process presents several significant advantages that make it superior against catalysts such as Ti-$LaFeO_3$ and (Ti:Ni) mixed-MOF in the degradation of carbofuran. Firstly, this catalyst generates hydroxyl radicals (HO•) directly and efficiently through the activation of H_2O_2, which enhances its effectiveness in contaminant degradation. Additionally, its high Cu^+/Cu^{2+} ratio improves electron transfer and ensures the continuous generation of reactive oxygen species (ROS) across a wide pH range. A crucial aspect is that the La(0.75) AH2-Cu perovskite structure contains oxygen vacancies, which increase its reactivity. This feature is further reinforced by the presence of lanthanum vacancies, which promote the release of oxygen from the crystal lattice. Structurally, the perovskite is stable, ensuring high durability of the catalyst across multiple reaction cycles. Finally, the copper present in the perovskite can be easily regenerated, allowing sustained catalytic activity without the need for specific operational conditions, such as exposure to ultraviolet light.

In contrast, the Ti-$LaFeO_3$ catalyst has some limitations. Firstly, the iron (Fe) sites in Ti-$LaFeO_3$, which are important for generating hydroxyl radicals, become less effective as the pH increases. Therefore, when operating under more acidic conditions, there is a greater likelihood of leaching of Fe active sites, which can affect catalytic performance. Furthermore, this catalyst lacks lanthanum vacancies, which are very useful for generating oxygen vacancies (OVs). Additionally, such study required higher doses of H_2O_2 (>100 % of the stoichiometric percentage for COD oxidation in the reaction medium), which can lead to secondary reactions that negatively impact process efficiency. Excess H_2O_2 can act as a scavenger for the formed hydroxyl radicals, generating less reactive radicals and thus reducing the effective concentration of HO• available for contaminant degradation [96]. Moreover, Ti-$LaFeO_3$ relies on UV light to activate the photo-Fenton reactions necessary for generating hydroxyl radicals, which can be a limitation in environments where UV light is not readily available or practical.

Similarly, MOF-based catalysts, such as those containing Ti and Ni used in photocatalysis, have some disadvantages. The generation of ROS in these materials depends on light absorption and complex charge transfer processes, which may be less efficient compared to the direct activation of H_2O_2 in the perovskite catalyst. Charge transfer in MOFs is subjected to the interaction between Ti, Ni, and organic ligands, with a higher likelihood of electron and hole recombination, reducing the efficiency in generating reactive species. Additionally, the porous and organic structure of MOFs does not leverage oxygen vacancies as a key factor in catalytic activity, limiting their ability to effectively generate ROS. The structural stability of MOFs is also inferior, being more susceptible to degradation under certain conditions, which can affect their reusability. Regeneration of MOFs is more complicated due to the tendency for charge carrier recombination.

On the other hand, with regard to the control experiments (Fig. 8a), direct attack of the oxidizing agent in the absence of catalyst (denoted as hydrogen peroxide) resulted in less than 26 % degradation and less than 13 % COD mineralization after reaction for 180 min (Table 4). Similarly, based on the results of catalyst adsorption, it can neither explain more than 31 % of the observed CBF degradation and 14 % of COD mineralization (Table 4). Under optimal reaction conditions, the system exhibits the highest apparent rate constant ($k = 0.0131\ min^{-1}$) upon comparison with the control experiments in the presence of hydrogen peroxide ($k = 0.0014\ min^{-1}$) or just catalyst adsorption ($k = 0.0017\ min^{-1}$) (Fig. 8b). This confirms that the catalytic activity exhibited by La(0.75)AH2-Cu prepared from Al saline slags, modified with Cu, and applied in the CWPO reaction, can be extensively attributed to the incorporation of Cu^+ metal centers strongly bonded within the perovskite crystal lattice, the generation of O vacancies due to both the cationic substitution of Al by Cu, and La deficiency. The small particle size of the catalyst, the structural distortion of the perovskite lattice, and the high purity and crystallinity of the synthesized material also play a relevant role. In light of the above, a plausible mechanism for CBF degradation and its interaction with the La(0.75)AH2-Cu catalyst in the presence of H_2O_2 can be proposed, as shown in Fig. 9. In this case, the activation of hydrogen peroxide (H_2O_2) on the catalyst surface involves the following stages: (*i*) The Cu^+ ions, due to their high electron density, interact with H_2O_2, reducing it to hydroxyl radicals (HO•), which are potent oxidizing agents essential for degrading contaminants like carbofuran. (*ii*) The oxidized Cu^{2+} can be reduced back to Cu^+ by reacting with intermediate organic compounds, ensuring a continuous cycle of radical generation. The stable oxygen bridges between neighboring copper ions facilitate electron transfer and support the redox cycling of Cu^{2+} to Cu^+. (*iii*) The presence of oxygen vacancies (OVs) in the catalyst facilitates the dissociation of H_2O_2 and the generation of HO• through a surface confinement pathway [77]. This synergistic combination of factors ensures high catalytic efficiency and stability across multiple reaction cycles, making the La(0.75)AH2-Cu catalyst highly effective in the CWPO process.

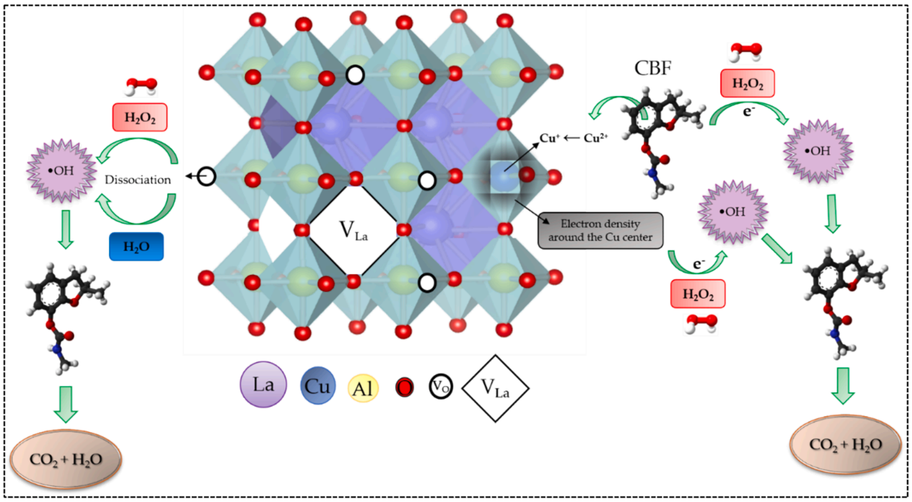

Fig. 9. Schematic illustration of the interaction of La(0.75)AH2-Cu with H_2O_2 and CBF.

According to published data [38,97,98], the possible reactions involved in the Fenton-like system catalyzed by copper species would be the following:

$$Cu^{+} + H_2O_2 \rightarrow Cu^{2+} + HO\bullet + HO^{-} \quad (8)$$

$$Cu^{2+} + H_2O_2 \rightarrow Cu^{+} + HO_2^{\bullet} + H^{+} \quad (9)$$

$$Cu^{2+} + HO_2^{\bullet} \rightarrow Cu^{+} + H^{+} + O_2 \quad (10)$$

$$Cu^{+} + HO_2^{\bullet} + H_2O_2 \rightarrow Cu^{+} + O_2 + HO\bullet + H_2O \quad (11)$$

$$Cu^{+} + H^{+} + H_2O_2 \rightarrow Cu^{2+} + HO\bullet + H_2O \quad (12)$$

Based on the reactions described above, both Cu^{2+} and Cu^{+} exhibit Fenton activity, generating $HO_2^{\bullet}$ and HO• radicals through Eqs. (8) and (9), respectively [38,98,99].

Fig. 8a shows that after reaction for 240 min, a maximum COD mineralization of 51.0 % was achieved. This indicates partial mineralization of the COD from both CBF and NOM into CO_2 and H_2O. As such, complete COD mineralization may require a longer reaction time. This might allow further degradation of the starting contaminants by active oxidizing species, which continuously attack these intermediates until the contaminant, NOM, and its byproducts could be entirely transformed into CO_2 and water [94]. The degradation pathway for CBF, which proceeds via oxidation by radical species including HO• and involves multiple transformations of intermediate products, has been reported in the literature [54,100–102] (Fig. S10). The CBF peak (*m/z* 221), designated as P1, has been identified in the original CBF solution. As the degradation progresses, new intermediates are formed via three main routes. In the first route, the attack of hydroxyl radicals (HO•) on the C–O bond in the carbamate group P1 leads to the formation of P2 (*m/z* 164), which generates additional products such as P5, P6, P7, P8, P9, P10 and P11 via demethylation reactions, ring opening, successive decarboxylations, and hydrolysis. In the second route, demethylation of P1 generates P3 (*m/z* 193), which is transformed into additional products such as P12, P13, P14 and P15 via hydroxylation reactions, further ring opening, decarboxylation, and hydrolysis. In the third route, P1 is transformed into P4 (*m/z* 237) by H abstraction and OH substitution in the furan ring. These routes represent the sequential transformations of CBF during the oxidation process and provide a detailed view of the intermediates formed.

The theoretical quantity of hydrogen peroxide consumed (assuming it reacts completely at the same rate as it is added to the reactor) with the optimal experimental test using La(0.75)AH2-Cu as catalyst is compared in Fig. 8c. The results show a high H_2O_2 conversion (71.2 %) after 180 min of reaction, which explains the optimal response for the heterogeneous Fenton degradation of the agrochemical and demonstrates a strong correlation between peroxide consumption and the best catalytic performance in contaminant degradation. As the quantity of oxidizing agent is below the theoretical value expected for stoichiometric transformation by molecular H_2O_2, the explanation for the high reaction yield achieved implies the formation of highly oxidizing species, including the aforementioned hydroxyl radical, whereas the efficiency of the H_2O_2 consumption is maximized towards ROS, in detrimental role of the parasites reactions wasting the oxidizing agent, that become more important as the pH of reaction rises.

Three sequential catalytic tests of the La(0.75)AH2-Cu catalyst (Optimum (exp), Reuse 1 and Reuse 2) were conducted to evaluate its reusability and stability in a prolonged operation under the optimal reaction conditions (Table 4). The CBF degradation observed in the three cycles was 94.1 %, 86.1 % (Reuse 1), and 80.1 % (Reuse 2), while the mineralization was 41.7 %, 36.0 % and 32.4 %, respectively, thus revealing moderate stability and the possibility of reuse. The stability of the catalyst was attributed to the low Cu leaching, as shown in Table 4. The Cu concentration cycle was initially 0.83 mg L^{-1}, increasing slightly to 1.20 mg L^{-1} and up to 1.30 mg L^{-1}. These concentrations still comply with US and EU regulations for drinking water [10]. The high chemical stability of the La(0.75)AH2-Cu catalyst against the leaching of Cu active sites can be attributed to its unique structure and the operating conditions used in the Catalytic Wet Peroxide Oxidation process (CWPO). Specifically, the high stability of copper in the perovskite lattice is due to several key factors: (*i*) The H_2-TPR results revealed that Cu in the La(0.75)AH2-Cu catalyst is strongly incorporated into the perovskite structure. The presence of reduction peaks at elevated temperatures (above 363 °C) suggests that Cu is strongly bonded to the crystal lattice, limiting its release during the catalytic process. This contrasts with other catalysts characterized, where Cu gets mainly stabilized as extra-framework oxides (CuO_x), which can be more susceptible to leaching (*ii*) The catalyst operates efficiently under near-neutral pH conditions, which is appropriate for minimizing Cu leaching. By maintaining a near-neutral pH, the La(0.75)AH2-Cu catalyst preserves its structural and functional integrity. (*iii*) The low Cu leaching (slightly increasing to 1.30 mg L^{-1} after two reuses) was an important factor. Furthermore, it was demonstrated that catalytic efficiency is maintained over several reaction cycles. This ensures that the catalyst does not lose activity over time, avoiding the need for frequent replacements, at least during three consecutive uses. Additionally, the leaching levels comply with regulatory standards for drinking water in both the US and the EU, which is essential to ensure that the use of this catalyst does not compromise the quality of treated water.

Additionally, it should be noted that both Cu^{+} and Cu^{2+} are fundamental to the function of the catalyst. The Cu^{+}/Cu^{2+} ratio is important because it supports a continuous and efficient redox cycle, which is essential for the sustained generation of hydroxyl radicals (HO•). These radicals are the primary agents responsible for degrading carbofuran. Therefore, the presence of both Cu^{+} and Cu^{2+} is necessary for the optimal performance of the catalyst in the CWPO process. Furthermore, based on the Eqs. (8) to (12) described above, both Cu^{2+} and Cu^{+} exhibit Fenton activity, generating $HO_2^{\bullet}$ and HO• radicals. However, a high content of Cu^{+} is especially important. Cu^{+} ions, due to their high electron density, interact effectively with H_2O_2, reducing it to hydroxyl radicals (HO•) and thereby enhancing the efficiency of the process. Consequently, a higher Cu^{+}/Cu^{2+} ratio can maximize the catalytic performance of the catalyst.

The decrease in the percentage of peroxide consumed (%) was very low, going from 71.2 % to 69.4 % (Table 4), thus indicating that the Cu active sites continue to contribute to the formation of highly oxidizing species even after the catalyst has been reused. In contrast, the gradual loss of CBF degradation efficiency could potentially be attributed to the accumulation of CBF [54], NOM [47], or their transformation products on the active sites of the catalyst. García-Mora *et al* [47], reported the presence of reversibly adsorbed carbonaceous residues from NOM, which could obstruct the external surface of the catalyst, in a reused Al/Fe-PILC type catalyst at near-neutral pH. This suggests that it may be necessary to pre-activate the catalyst prior to reuse in order to maintain higher efficiency in subsequent cycles.

Finally, after evaluating the catalytic performance of the La(1.0)AH2-Cu catalyst under optimal conditions for CBF degradation (see Fig. S11 and Table 4), a 79.4 % CBF degradation, 32.5 % COD mineralization, 50.0 % hydrogen peroxide consumption, and 1.03 mg L^{-1} of leached Cu were achieved at 25 °C after 180 min of reaction, with a DOC concentration of 20.4 mg L^{-1}. However, this catalyst exhibited lower catalytic performance compared to the La(0.75)AH2-Cu catalyst. The latter demonstrated superior performance due to the synergy of its enhanced physicochemical properties. La(0.75)AH2-Cu exhibited higher purity of the perovskite phase obtained, as well as improved textural properties, including a larger specific surface area and a greater total pore volume. These characteristics resulted in a higher number of available active sites and better diffusion of reactants and products within and outside the catalyst structure. Additionally, the lower amount of leached Cu corroborates the H_2-TPR results, supporting the high stability of the incorporated octahedral Cu in the absence of impurities, such as La_2CuO_4, that could affect its stability and catalytic performance. Moreover, the preparation of the La(0.75)AH2-Cu catalyst with La deficiency significantly contributed to the generation of oxygen vacancies and the control of the average Cu valence state, favoring a high proportion of Cu^+ active sites effectively dispersed within the perovskite structure. These sites, along with the oxygen vacancies, contributed to the reduction of H_2O_2 and the formation of reactive oxygen species, such as the hydroxyl radical (HO•). It is worth noting that it has been demonstrated that Cu^{2+} stabilized in structures such as La_2CuO_4, which was identified in the La(1.0)AH2-Cu catalyst, produces a slower decomposition of H_2O_2 [38]. Therefore, these combined characteristics led to enhanced catalytic performance.

4. Conclusions

Perovskite-type $La_yAl_{1-x}Cu_xO_{3-\delta}$ catalysts with high purity (up to 90 %) were successfully synthesized and here reported for the first time using Al efficiently recovered by acid leaching of a saline slag. Adjustment of the La/Al molar ratio allowed simultaneous control of purity, La and O vacancies, as well as the average Cu valence state. The La(0.75)AH2-Cu catalyst exhibited optimal performance, with a high concentration of Cu(I) active sites effectively dispersed within the perovskite lattice. This resulted in a decreased particle size, increased surface roughness, and the absence of extra-framework metal oxides.

Wet peroxide oxidation activated by the La(0.75)AH2-Cu catalyst achieved optimal CBF degradation (94.1 %) under ambient conditions (25 °C and 1 atm). Key factors such as catalyst concentration, peroxide dosage, and pH were optimized using response surface methodology and a statistical desirability multi-response function. This approach maximized degradation efficiency, COD mineralization, and hydrogen peroxide consumption, while minimizing Cu leaching.

The low dosage of H_2O_2 required (just over a half the predicted amount) and the stability of the catalyst during reuse (up to three cycles) further highlight its potential. The optimal reaction conditions closely resemble real wastewater conditions (close to neutral pH, temperature, and initial COD), thus making La(0.75)AH2-Cu a promising material for efficient treatment of industrial wastewater.

CRediT authorship contribution statement

H.J. Muñoz: Writing – original draft, Investigation, Formal analysis, Conceptualization. **L.A. Galeano:** Writing – original draft, Conceptualization. **M.A. Vicente:** Writing – review & editing, Writing – original draft, Validation, Conceptualization. **S.A. Korili:** Writing – review & editing, Resources, Project administration, Investigation. **A. Gil:** Writing – review & editing, Writing – original draft, Supervision, Resources, Project administration, Funding acquisition, Conceptualization.

Declaration of competing interest

The authors declare that they have no known competing financial interests or personal relationships that could have appeared to influence the work reported in this paper.

Data availability

No data was used for the research described in the article.

Acknowledgments

The authors are grateful for financial support from the Spanish Ministry of Science and Innovation (MCIN/AEI/10.13039/501100011033) through projects PID2020-112656RB-C21 and PID2023-146935OB-C21. HJM thanks the Universidad Pública de Navarra for a doctoral grant. Open access funding provided by Universidad Pública de Navarra.

Appendix A. Supplementary data

Supplementary data to this article can be found online at https://doi.org/10.1016/j.cej.2024.155971.

References

[1] M. Samy, A.G. Kumi, E. Salama, M. ElKady, K. Mensah, H. Shokry, Heterogeneous activation of persulfate by a novel nano-magnetite/ZnO/activated carbon nanohybrid for carbofuran degradation: Toxicity assessment, water matrices, degradation mechanism and radical and non-radical pathways, Process Saf. Environ. Prot. 169 (2023) 337–351, https://doi.org/10.1016/j.psep.2022.11.038.

[2] S. Stehle, S. Bub, R. Schulz, Compilation and analysis of global surface water concentrations for individual insecticide compounds, Sci. Total Environ. 639 (2018) 516–525, https://doi.org/10.1016/j.scitotenv.2018.05.158.

[3] N. Lopez-Herguedas, B. González-Gaya, N. Castelblanco-Boyacá, A. Rico, N. Etxebarria, M. Olivares, A. Prieto, O. Zuloaga, Characterization of the contamination fingerprint of wastewater treatment plant effluents in the Henares River Basin (central Spain) based on target and suspect screening analysis, Sci. Total Environ. 806 (2022) 151262, https://doi.org/10.1016/j.scitotenv.2021.151262.

[4] A. Abdelhaleem, W. Chu, Prediction of carbofuran degradation based on the hydroxyl radical's generation using the Fe^{III} impregnated N doped-TiO_2/H_2O_2/visible LED photo-Fenton-like process, Chem. Eng. J. 382 (2020) 122930, https://doi.org/10.1016/j.cej.2019.122930.

[5] L.A. Lu, Y.S. Mab, M. Kumar, J.G. Lin, Photo-fenton pretreatment of carbofuran -analyses via experimental design, detoxification and biodegradability enhancement, Sep. Purif. Technol. 81 (2011) 325–331, https://doi.org/10.1016/j.seppur.2011.07.040.

[6] M.U. Mustapha, N. Halimoon, W.L.W. Johari, M.Y.A. Shukor, Enhanced carbofuran degradation using immobilized and free cells of Enterobacter sp. isolated from soil, Molecules. 25 (2020) 2771, https://doi.org/10.3390/molecules25122771.

[7] A.S. Mansano, R.A. Moreira, H.C. Dornfeld, L.G.R. Diniz, E.M. Vieira, M.A. Daam, O. Rocha, M.H.R. Seleghim, Acute and chronic toxicity of diuron and carbofuran to the neotropical cladoceran Ceriodaphnia silvestrii, Environ. Sci. Pollut. Res. 25 (2018) 13335–13346, https://doi.org/10.1007/s11356-016-8274-9.

[8] P. Rajiv, R. Manikandan, S. Sangeetha, P. Vanathi, S. Dhanasekaran, Fabrication of biogenic iron oxide and their efficiency to detect carbofuran in vegetable samples, Inorg. Chem. Commun. 142 (2022) 109649, https://doi.org/10.1016/j.inoche.2022.109649.

[9] V. Mariyappan, M. Keerthi, S.M. Chen, Highly selective electrochemical sensor based on gadolinium sulfide rod-embedded RGO for the sensing of carbofuran, J. Agric. Food Chem. 69 (2021) 2679–2688, https://doi.org/10.1021/acs.jafc.0c07522.

[10] H. Wang, L. Zhang, C. Hu, X. Wang, L. Lyu, G. Sheng, Enhanced degradation of organic pollutants over Cu-doped $LaAlO_3$ perovskite through heterogeneous Fenton-like reactions, Chem. Eng. J. 332 (2018) 572–581, https://doi.org/10.1016/j.cej.2017.09.058.

[11] H.J.H. Fenton, LXXIII.—Oxidation of tartaric acid in presence of iron, J. Chem. Soc. Trans. 65 (1894) 899–910, https://doi.org/10.1039/CT8946500899.

[12] M. Munoz, Z.M. de Pedro, J.A. Casas, J.J. Rodriguez, Preparation of magnetite-based catalysts and their application in heterogeneous Fenton oxidation - A review, Appl. Catal. B Environ. 176–177 (2015) 249–265, https://doi.org/10.1016/j.apcatb.2015.04.003.

[13] Z. Wang, C. Fang, M. Megharaj, Characterization of iron-polyphenol nanoparticles synthesized by three plant extracts and their fenton oxidation of azo dye, ACS Sustain. Chem. Eng. 2 (2014) 1022–1025, https://doi.org/10.1021/sc500021n.

[14] Z. Zuo, H. Lv, R. Li, F. Liu, H. Zhao, A new approach to recover the valuable elements in black aluminum dross, Resour. Conserv. Recycl. 174 (2021) 105768, https://doi.org/10.1016/j.resconrec.2021.105768.

[15] Y. Li, Z. Qin, C. Li, Y. Qu, H. Wang, L. Peng, Y. Wang, Hazardous characteristics and transformation mechanism in hydrometallurgical disposing strategy of secondary aluminum dross, J. Environ. Chem. Eng. 9 (2021) 106470, https://doi.org/10.1016/j.jece.2021.106470.

[16] A. Gil, S.A. Korili, Management and valorization of aluminum saline slags: Current status and future trends, Chem. Eng. J. 289 (2016) 74–84, https://doi.org/10.1016/j.cej.2015.12.069.

[17] A. Gil, Management of the salt cake from secondary aluminum fusion processes, Ind. Eng. Chem. Res. 44 (2005) 8852–8857, https://doi.org/10.1021/ie050835o.

[18] J.J. Torrez-Herrera, E.G. Fuentes-Ordoñez, S.A. Korili, A. Gil, Evidence for the synthesis of La-hexaaluminate from aluminum-containing saline slag wastes: Correction of structural defects and phase purification at low temperature, Powder Technol. 377 (2021) 80–88, https://doi.org/10.1016/j.powtec.2020.08.087.

[19] J.J. Torrez-Herrera, S.A. Korili, A. Gil, Structure and activity of nickel supported on hibonite-type La-hexaaluminates synthesized from aluminum saline slags for the dry reforming of methane, Chem. Eng. J. Adv. 5 (2021) 100080, https://doi.org/10.1016/j.ceja.2020.100080.

[20] Y. Cardona, S.A. Korili, A. Gil, A nonconventional aluminum source in the production of alumina-pillared clays for the removal of organic pollutants by

adsorption, Chem. Eng. J. 425 (2021) 130708, https://doi.org/10.1016/j.cej.2021.130708.

[21] J.J. Torrez-Herrera, S.A. Korili, A. Gil, Bimetallic (Pt-Ni) La-hexaaluminate catalysts obtained from aluminum saline slags for the dry reforming of methane, Chem. Eng. J. 433 (2022) 133191, https://doi.org/10.1016/j.cej.2021.133191.

[22] A. Jiménez, B.M. Esteves, R. Trujillano, M.A. Soria, L.M. Madeira, V. Rives, M.Á. Vicente, Tyrosol removal by photo–Fenton–like process using CaAlFe mixed oxides synthesized via hydrocalumite from aluminum salt cake, J. Environ. Chem. Eng. 12 (2024), https://doi.org/10.1016/j.jece.2024.112423.

[23] A. Gil, Challenges on waste-to-energy for the valorization of industrial wastes: Electricity, heat and cold, bioliquids and biofuels, Environ. Nanotechnol., Monit. Manag. 17 (2022) 100615, https://doi.org/10.1016/j.enmm.2021.100615.

[24] D. Brough, H. Jouhara, The aluminium industry: A review on state-of-the-art technologies, environmental impacts and possibilities for waste heat recovery, Int. J. Thermofluids. 1–2 (2020), https://doi.org/10.1016/j.ijft.2019.100007.

[25] M. Yoldi, E.G. Fuentes-Ordoñez, S.A. Korili, A. Gil, Efficient recovery of aluminum from saline slag wastes, Miner. Eng. 140 (2019) 105884, https://doi.org/10.1016/j.mineng.2019.105884.

[26] A. Jiménez, V. Rives, M.A. Vicente, A. Gil, A comparative study of acid and alkaline aluminum extraction valorization procedure for aluminum saline slags, J. Environ. Chem. Eng. 10 (2022) 1–10, https://doi.org/10.1016/j.jece.2022.107546.

[27] A. Vallejo Olivares, E. Pastor-Vallés, J.B. Pettersen, G. Tranell, LCA of recycling aluminium incineration bottom ash, dross and shavings in a rotary furnace and environmental benefits of salt-slag valorisation, Waste Manag. 182 (2024) 11–20, https://doi.org/10.1016/j.wasman.2024.04.023.

[28] L. Santamaría, F. Devred, E.M. Gaigneaux, M.A. Vicente, S.A. Korili, A. Gil, Effect of the surface properties of Me^{2+}/Al layered double hydroxides synthesized from aluminum saline slag wastes on the adsorption removal of drugs, Microporous Mesoporous Mater. 309 (2020) 110560, https://doi.org/10.1016/j.micromeso.2020.110560.

[29] A. Gil, E. Arrieta, M.A. Vicente, S.A. Korili, Synthesis and CO_2 adsorption properties of hydrotalcite-like compounds prepared from aluminum saline slag wastes, Chem. Eng. J. 334 (2018) 1341–1350, https://doi.org/10.1016/j.cej.2017.11.100.

[30] A. Jiménez, A. Misol, Á. Morato, V. Rives, M.A. Vicente, A. Gil, Optimization of hydrocalumite preparation under microwave irradiation for recovering aluminium from a saline slag, Appl. Clay Sci. 212 (2021), https://doi.org/10.1016/j.clay.2021.106217.

[31] M. Yoldi, E.G. Fuentes-Ordoñez, S.A. Korili, A. Gil, Zeolite synthesis from aluminum saline slag waste, Powder Technol. 366 (2020) 175–184, https://doi.org/10.1016/j.powtec.2020.02.069.

[32] A. Jiménez, A. Misol, Á. Morato, V. Rives, M.A. Vicente, A. Gil, Synthesis of pollucite and analcime zeolites by recovering aluminum from a saline slag, J. Clean. Prod. 297 (2021), https://doi.org/10.1016/j.jclepro.2021.126667.

[33] J.J. Torrez-Herrera, S.A. Korili, A. Gil, Development of ceramic-MOF filters from aluminum saline slags for capturing CO_2, Powder Technol. 429 (2023) 118962, https://doi.org/10.1016/j.powtec.2023.118962.

[34] X. Zhang, L. Zhang, C. Hu, M. Yang, Enhanced •OH generation and pollutants removal by framework Cu doped $LaAlO_3/Al_2O_3$, J. Hazard. Mater. 431 (2022) 128578, https://doi.org/10.1016/j.jhazmat.2022.128578.

[35] H.J. Muñoz, S.A. Korili, A. Gil, Progress and recent strategies in the synthesis and catalytic applications of perovskites based on lanthanum and aluminum, Materials (Basel). 15 (2022) 3288. https:// doi.org/10.3390/ma15093288.

[36] J. Li, D. Zhong, Y. Gan, Z. Li, Y. Cao, W. Ma, K. Li, J. Li, Oxygen vacancy mediated Ruddlesden-Popper Cu-based perovskites wih a dual-reaction-center for enhanced fenton-like removal of coal pyrolysis wastewater, Sep. Purif. Technol. 338 (2024) 126449, https://doi.org/10.1016/j.seppur.2024.126449.

[37] A. Abdelhaleem, H.N. Abdelhamid, M.G. Ibrahim, W. Chu, Photocatalytic degradation of paracetamol using photo-Fenton-like metal-organic framework-derived CuO@C under visible LED, J. Clean. Prod. 379 (2022) 134571, https://doi.org/10.1016/j.jclepro.2022.134571.

[38] M.R. Carrasco-Díaz, E. Castillejos-López, A. Cerpa-Naranjo, M.L. Rojas-Cervantes, Efficient removal of paracetamol using $LaCu_{1-x}M_xO_3$ (M = Mn, Ti) perovskites as heterogeneous Fenton-like catalysts, Chem. Eng. J. 304 (2016) 408–418, https://doi.org/10.1016/j.cej.2016.06.054.

[39] Y. Gao, B. Jiang, X. Shi, J. He, W. Si-ma, C. Huang, L. Li, D. Tang, A-site vacancy induced electronic engineering of perovskite for synergistic modulation of redox activity and magnetocaloric effect, Nano Energy. 117 (2023) 108912, https://doi.org/10.1016/j.nanoen.2023.108912.

[40] Z. Fang, X. Feng, Z. Zhou, Z. Zeng, Y. Xia, J. Li, J. Liu, B. Hu, K. Li, Q. Lu, Cation defect engineering in $LaCoO_3$ perovskite as the "Two birds one stone" strategy to enhanced Fenton-like reaction: Regulating Co spin state and optimizing electron transfer ability, Sep. Purif. Technol. 337 (2024) 126417, https://doi.org/10.1016/j.seppur.2024.126417.

[41] O.P. Taran, A.B. Ayusheev, O.L. Ogorodnikova, I.P. Prosvirin, L.A. Isupova, V. N. Parmon, Perovskite-like catalysts LaBO3 (B=Cu, Fe, Mn Co, Ni) for wet peroxide oxidation of phenol, Appl. Catal. B Environ. 180 (2016) 86–93, https://doi.org/10.1016/j.apcatb.2015.05.055.

[42] F. Benstoem, A. Nahrstedt, M. Boehler, G. Knopp, D. Montag, H. Siegrist, J. Pinnekamp, Performance of granular activated carbon to remove micropollutants from municipal wastewater—A meta-analysis of pilot- and large-scale studies, Chemosphere. 185 (2017) 105–118, https://doi.org/10.1016/j.chemosphere.2017.06.118.

[43] M. Campinas, R.M.C. Viegas, C.M.M. Almeida, A. Martins, C. Silva, E. Mesquita, M.R. Coelho, S. Silva, V.V. Cardoso, M.J. Benoliel, M.J. Rosa, Powdered activated carbon full-scale addition to the activated sludge reactor of a municipal wastewater treatment plant: Pharmaceutical compounds control and overall impact on the process, J. Water Process Eng. 49 (2022) 102975, https://doi.org/10.1016/j.jwpe.2022.102975.

[44] J.J. Rueda-Marquez, I. Levchuk, P. Fernández Ibañez, M. Sillanpää, A critical review on application of photocatalysis for toxicity reduction of real wastewaters, J. Clean. Prod. 258 (2020) 120694. https://doi.org/10.1016/j.jclepro.2020.120694.

[45] L. Bouchaala, N. Charchar, H. Sahraoui, A. Gherib, Assessment of wastewater biological treatment efficiency and mapping of WWTPs and LTPs in Algeria, J. Environ. Heal. Sci. Eng. 19 (2021) 1153–1169, https://doi.org/10.1007/s40201-021-00682-1.

[46] Y. Cohen, H. Kirchmann, Increasing the pH of wastewater to high levels with different gases - CO_2 stripping, Water. Air. Soil Pollut. 159 (2004) 265–275, https://doi.org/10.1023/B:WATE.0000049185.69759.b0.

[47] A.M. Garcia-Mora, R.A. Torres-Palma, H. García, A. Hidalgo-Troya, L.A. Galeano, Removal of dissolved natural organic matter by the Al/Fe pillared clay-activated-catalytic wet peroxide oxidation: Statistical multi-response optimization, J. Water Process Eng. 39 (2021) 101755, https://doi.org/10.1016/j.jwpe.2020.101755.

[48] G. Lee, I. Kim, I. Yang, J.M. Ha, H. Bin Na, J.C. Jung, Effects of the preparation method on the crystallinity and catalytic activity of $LaAlO_3$ perovskites for oxidative coupling of methane, Appl. Surf. Sci. 429 (2018) 55–61. https://doi.org/10.1016/j.apsusc.2017.08.092.

[49] J. Rouquerol, F. Rouquerol, P. Llewellyn, G. Maurin, K.S.W. Sing, Adsorption by Powders and Porous Solids: Principles, Methodology and Applications, Academic Press, The Netherlands, 2013.

[50] H.J. Muñoz, C. Vallejo, C. Blanco, A. Gil, M.Á. Vicente, J.H. Ramírez, L. A. Galeano, 10 kg scaled-up preparation of Al/Fe-pillared clay CWPO catalysts from concentrated precursors, Green Chem. 20 (2018) 5196–5208, https://doi.org/10.1039/c8gc02445f.

[51] N. Her, G. Amy, H.R. Park, M. Song, Characterizing algogenic organic matter (AOM) and evaluating associated NF membrane fouling, Water Res. 38 (2004) 1427–1438, https://doi.org/10.1016/j.watres.2003.12.008.

[52] H. Park, Y. Kim, B. An, H. Choi, Characterization of natural organic matter treated by iron oxide nanoparticle incorporated ceramic membrane-ozonation process, Water Res. 46 (2012) 5861–5870, https://doi.org/10.1016/j.watres.2012.07.039.

[53] M.D. Kennedy, H.K. Chun, V.A. Quintanilla Yangali, B.G.J. Heijman, J.C. Schippers, Natural organic matter (NOM) fouling of ultrafiltration membranes: Fractionation of NOM in surface water and characterisation by LC-OCD, Desalination. 178 (2005) 73–83. https://doi.org/10.1016/j.desal.2005.02.004.

[54] K. Fouad, M. Gar Alalm, M. Bassyouni, M.Y. Saleh, Optimization of catalytic wet peroxide oxidation of carbofuran by Ti-$LaFeO_3$ dual photocatalyst, Environ. Technol. Innov. 23 (2021) 101778. https://doi.org/10.1016/j.eti.2021.101778.

[55] L.A. Galeano, P.F. Bravo, C.D. Luna, M.Á. Vicente, A. Gil, Removal of natural organic matter for drinking water production by Al/Fe-PILC-catalyzed wet peroxide oxidation: Effect of the catalyst preparation from concentrated precursors, Appl. Catal. B Environ. 111 (2012) 527–535, https://doi.org/10.1016/j.apcatb.2011.11.004.

[56] N.V. Klassen, D. Marchington, H.C.E. McGowan, H_2O_2 determination by the I_3^- method and by $KMnO_4$ titration, Anal. Chem. 66 (1994) 2921–2925, https://doi.org/10.1021/ac00090a020.

[57] W. Ma, S. Zhang, L. Deng, D. Zhong, K. Li, X. Liu, J. Li, J. Zhang, J. Ma, Cu-based perovskite as a novel CWPO catalyst for petroleum refining wastewater treatment: Performance, toxicity and mechanism, J. Hazard. Mater. 448 (2023) 130824, https://doi.org/10.1016/j.jhazmat.2023.130824.

[58] T. Chen, Z. Zhu, Z. Wang, H. Zhang, Y. Qiu, D. Yin, G. Zhao, 3D hollow sphere-like Cu-incorporated $LaAlO_3$ perovskites for peroxymonosulfate activation: Coaction of electron transfer and oxygen defect, Chem. Eng. J. 385 (2020) 123935, https://doi.org/10.1016/j.cej.2019.123935.

[59] Y. Rao, Y. Zhang, J. Fan, G. Wei, D. Wang, F. Han, Y. Huang, J.P. Croué, Enhanced peroxymonosulfate activation by Cu-doped LaFeO3 with rich oxygen vacancies: compound-specific mechanisms, Chem. Eng. J. 435 (2022) 134882, https://doi.org/10.1016/j.cej.2022.134882.

[60] M. Li, M. Feng, C. Guo, S. Qiu, L. Zhang, D. Zhao, H. Guo, K. Zhang, F. Wang, Green and efficient Al-Doped $LaFe_xAl_{1-x}O_3$ perovskite oxide for enhanced phosphate adsorption with creation of oxygen vacancies, ACS Appl. Mater. Interfaces. 15 (2023) 16942–16952, https://doi.org/10.1021/acsami.2c19513.

[61] T.T.N. Phan, A.N. Nikoloski, P.A. Bahri, D. Li, Heterogeneous photo-Fenton degradation of organics using highly efficient Cu-doped $LaFeO_3$ under visible light, J. Ind. Eng. Chem. 61 (2018) 53–64, https://doi.org/10.1016/j.jiec.2017.11.046.

[62] H.J. Muñoz, S.A. Korili, A. Gil, Facile synthesis of an Ni/LaAlO3 – Perovskite via an MOF gel precursor for the dry reforming of methane, Catal. Today. 429 (2023) 114487, https://doi.org/10.1016/j.cattod.2023.114487.

[63] I.S. Silveira, N.S. Ferreira, D.N. Souza, Structural, morphological and vibrational properties of $LaAlO_3$ nanocrystals produced by four different methods, Ceram. Int. 47 (2021) 27748–27758, https://doi.org/10.1016/j.ceramint.2021.06.201.

[64] A.H. Martínez, E. Lopez, L.E. Cadús, F.N. Agüero, Elucidation of the role of support in Rh/perovskite catalysts used in ethanol steam reforming reaction, Catal. Today. 372 (2021) 59–69, https://doi.org/10.1016/j.cattod.2020.12.013.

[65] Y. Wu, T. She, Y. Wang, Z. Xu, T. Huang, Q. Ji, H. Song, S. Yang, S. Li, S. Yan, L. Zhang, H. He, Enhancing cationic superexchange interaction via adjustive lattice distortion in cobalt-based perovskite for improved Fenton-like decontamination, Appl. Catal. B Environ. 343 (2024) 123569, https://doi.org/10.1016/j.apcatb.2023.123569.

[66] C.A. Da Silva, P.E.V. De Miranda, Synthesis of $LaAlO_3$ based materials for potential use as methane-fueled solid oxide fuel cell anodes, Int. J. Hydrog. 40 (2015) 10002–10015, https://doi.org/10.1016/j.ijhydene.2015.06.019.

[67] Ł. Łańcucki, A. Mizera, A. Łkacz, E. Drożdż, M.M. Bućko, P. Pasierb, Development and chemical stability evaluation of enhanced surface $LaFe_{1-x}Ti_xO_3$ (LFT) perovskites using polystyrene nanospheres as templating agent, J. Alloys Compd. 727 (2017) 863–870.

[68] J. Zhang, J. Chen, Y. Luo, Y. Chen, C. Zhang, Y. Luo, Y. Xue, H. Liu, G. Wang, R. Wang, Engineering heterointerfaces coupled with oxygen vacancies in lanthanum–based hollow microspheres for synergistically enhanced oxygen electrocatalysis, J. Energy Chem. 60 (2021) 503–511, https://doi.org/10.1016/j.jechem.2020.11.037.

[69] F.E. López-Suárez, S. Parres-Esclapez, A. Bueno-López, M.J. Illán-Gómez, B. Ura, J. Trawczynski, Role of surface and lattice copper species in copper-containing (Mg/Sr)TiO_3 perovskite catalysts for soot combustion, Appl. Catal. B Environ. 93 (2009) 82–89, https://doi.org/10.1016/j.apcatb.2009.09.015.

[70] J. Li, D. Zhong, Y. Chen, K. Li, W. Ma, S. Zhang, J. Zhang, A. Sun, H. Xie, Copper-based Ruddlesden-Popper perovskite oxides activated hydrogen peroxide for coal pyrolysis wastewater (CPW) degradation: performance and mechanism, Environ. Res. 216 (2023) 114591, https://doi.org/10.1016/j.envres.2022.114591.

[71] B. Chen, J. Yu, X. Liang, $LaAlO_3$ hollow spheres: Synthesis and luminescence properties, Langmuir. 27 (2011) 11654–11659, https://doi.org/10.1021/la201889n.

[72] J. Lu, H. Liu, X. Zhao, W. Jefferson, F. Cheng, J. Qu, Phosphate removal from water using freshly formed Fe-Mn binary oxide: Adsorption behaviors and mechanisms, Colloids Surfaces A Physicochem. Eng. Asp. 455 (2014) 11–18, https://doi.org/10.1016/j.colsurfa.2014.04.034.

[73] Q. Ji, L. Bi, J. Zhang, H. Cao, X.S. Zhao, The role of oxygen vacancies of ABO_3 perovskite oxides in the oxygen reduction reaction, Energy Environ. Sci. 13 (2020) 1408–1428, https://doi.org/10.1039/d0ee00092b.

[74] L. Xie, X. Liu, J. Chang, C. Zhang, Y. Li, H. Zhang, S. Zhan, W. Hu, Enhanced redox activity and oxygen vacancies of perovskite triggered by copper incorporation for the improvement of electro-Fenton activity, Chem. Eng. J. 428 (2022), https://doi.org/10.1016/j.cej.2021.131352.

[75] A. Sato, S. Ogo, Y. Takeno, K. Takise, J.G. Seo, Y. Sekine, Electric field and mobile oxygen promote low-temperature oxidative coupling of methane over $La_{1-x}Ca_xAlO_{3-\delta}$ perovskite catalysts, ACS Omega. 4 (2019) 10438–10443, https://doi.org/10.1021/acsomega.9b00594.

[76] Y. Wang, R. Wang, L. Yu, Y. Wang, C. Zhang, X. Zhang, Efficient reactivity of $LaCu_{0.5}Co_{0.5}O_3$ perovskite intercalated montmorillonite and $g\text{-}C_3N_4$ nanocomposites in microwave-induced H_2O_2 catalytic degradation of bisphenol A, Chem. Eng. J. 401 (2020) 126057, https://doi.org/10.1016/j.cej.2020.126057.

[77] H. Li, J. Shang, Z. Yang, W. Shen, Z. Ai, L. Zhang, Oxygen vacancy associated surface fenton chemistry: surface structure dependent hydroxyl radicals generation and substrate dependent reactivity, Environ. Sci. Technol. 51 (2017) 5685–5694, https://doi.org/10.1021/acs.est.7b00040.

[78] W. Liu, Y. Zou, Y. Chen, Z. Lei, L. Zhao, L. Song, Optimizing the Structure and Optical Properties of Lanthanum Aluminate Perovskite through Nb^{5+} Doping, (2024).

[79] C. Fei, H. Liu, X. Wang, D. Zhao, S. Wang, Influences of rapid thermal annealing on the characteristics of $Al_2O_3\backslash La_2O_3\backslash Si$ and $La_2O_3\backslash Al_2O_3\backslash Si$ films deposited by atomic layer deposition, J. Mater. Sci. Mater. Electron. 27 (2016) 8550–8558, https://doi.org/10.1007/s10854-016-4872-z.

[80] Q. Wang, Y. Ma, S. Xing, Comparative study of Cu-based bimetallic oxides for Fenton-like degradation of organic pollutants, Chemosphere. 203 (2018) 450–456, https://doi.org/10.1016/j.chemosphere.2018.04.013.

[81] J. Cai, H. Gong, The influence of Cu/Al ratio on properties of chemical-vapor-deposition-grown p -type Cu-Al-O transparent semiconducting films, J. Appl. Phys. 98 (2005) 033707, https://doi.org/10.1063/1.1997293.

[82] S. Kasala, M.V. Sudandara Doss, Microwave assisted synthesis and powder flowability characteristics of rare-earth aluminate ($ReAlO_3$, Re = La, Gd, Nd, Y) powders, Trans. Indian Ceram. Soc. 78 (2019) 13–19. https://doi.org/10.1080/0371750X.2019.1566024.

[83] X. Cui, H. Yang, J. Zhang, T. Wu, P. Zhao, Q. Guo, Characterization and performance of Ca-substituted $La_{1-x}Ca_xCoO_{3-\delta}$ perovskite for efficient catalytic oxidation of toluene, Catal. Letters. 151 (2021) 3323–3333, https://doi.org/10.1007/s10562-021-03566-z.

[84] H. Yan, C.F. Blanford, B.T. Holland, W.H. Smyrl, A. Stein, General synthesis of periodic macroporous solids by templated salt precipitation and chemical conversion, Chem. Mater. 12 (2000) 1134–1141, https://doi.org/10.1021/cm9907763.

[85] M. Rafiq, A. Ahmed, M. Usman, R. Ullah, F. Gao, M. Mateen, B. Yu, Y. Shen, H. Cong, Efficient heterogeneous activation of peroxymonosulfate by manganese-doped $LaCoO_3$ perovskites for metronidazole degradation: A mechanistic study and reaction pathways, J. Environ. Chem. Eng. 11 (2023) 111608, https://doi.org/10.1016/j.jece.2023.111608.

[86] F. Jiang, D. Chen, Z. Wang, Z. Xu, J. Chen, L. Liu, Y. Huyan, Y. Liu, Pore characteristic analysis of a lacustrine shale: A case study in the Ordos Basin, NW China, Mar. Pet. Geol. 73 (2016) 554–571, https://doi.org/10.1016/j.marpetgeo.2016.03.026.

[87] K. Chen, T. Zhang, X. Chen, Y. He, X. Liang, Model construction of micro-pores in shale: A case study of Silurian Longmaxi Formation shale in Dianqianbei area, SW China, Pet. Explor. Dev. 45 (2018) 412–421, https://doi.org/10.1016/S1876-3804(18)30046-6.

[88] Y. Farhang, E. Taheri-Nassaj, M. Rezaei, Enhanced methane combustion and CO oxidation with Pd and Pt substitution $LaSrCuO_4$ perovskites, Mater. Today Commun. 36 (2023) 106891, https://doi.org/10.1016/j.mtcomm.2023.106891.

[89] M. Borowski, Perovskites: Structure, Properties, and Uses, Nova Science Publishers, 2010.

[90] V. Albaladejo-Fuentes, F.E. López-Suárez, M.S. Sánchez-Adsuar, M.J. Illán-Gómez, $BaTi_{1-x}Cu_xO_3$ perovskites: The effect of copper content in the properties and in the NO_x storage capacity, Appl. Catal. A Gen. 488 (2014) 189–199, https://doi.org/10.1016/j.apcata.2014.09.032.

[91] S. Thongratkaew, C. Luadthong, S. Kiatphuengporn, P. Khemthong, P. Hirunsit, K. Faungnawakij, Cu-Al spinel-oxide catalysts for selective hydrogenation of furfural to furfuryl alcohol, Catal. Today. 367 (2021) 177–188, https://doi.org/10.1016/j.cattod.2020.04.066.

[92] L. Mao, X. Zhao, Y. Xiao, G. Dong, The effect of the structure and oxygen defects on the simultaneous removal of NO_x and soot by $La_{2-x}Ba_xCuO_4$, New J. Chem. 43 (2019) 4196–4204, https://doi.org/10.1039/c8nj04233k.

[93] Q.N. Tran, F. Martinovic, M. Ceretti, S. Esposito, B. Bonelli, W. Paulus, F. Di Renzo, F.A. Deorsola, S. Bensaid, R. Pirone, Co-doped $LaAlO_3$ perovskite oxide for NOx-assisted soot oxidation, Appl. Catal. A Gen. 589 (2020) 117304, https://doi.org/10.1016/j.apcata.2019.117304.

[94] M. Samy, M. Gar Alalm, M. Fujii, M.G. Ibrahim, Doping of Ni in MIL-125(Ti) for enhanced photocatalytic degradation of carbofuran: Reusability of coated plates and effect of different water matrices, J. Water Process Eng. 44 (2021) 102449. https://doi.org/10.1016/j.jwpe.2021.102449.

[95] L. Lyu, L. Zhang, C. Hu, Galvanic-like cells produced by negative charge nonuniformity of lattice oxygen on d-TiCuAl-SiO_2 nanospheres for enhancement of Fenton-catalytic efficiency, Environ. Sci Nano. 3 (2016) 1483–1492, https://doi.org/10.1039/c6en00290k.

[96] J. Herney-Ramirez, M.A. Vicente, L.M. Madeira, Heterogeneous photo-Fenton oxidation with pillared clay-based catalysts for wastewater treatment: A review, Appl. Catal. B Environ. 98 (2010) 10–26, https://doi.org/10.1016/j.apcatb.2010.05.004.

[97] A.D. Bokare, W. Choi, Review of iron-free Fenton-like systems for activating H_2O_2 in advanced oxidation processes, J. Hazard. Mater. 275 (2014) 121–135, https://doi.org/10.1016/j.jhazmat.2014.04.054.

[98] A.N. Pham, G. Xing, C.J. Miller, T.D. Waite, Fenton-like copper redox chemistry revisited: Hydrogen peroxide and superoxide mediation of copper-catalyzed oxidant production, J. Catal. 301 (2013) 54–64, https://doi.org/10.1016/j.jcat.2013.01.025.

[99] L. Zhang, Y. Nie, C. Hu, J. Qu, Enhanced Fenton degradation of Rhodamine B over nanoscaled Cu-doped $LaTiO_3$ perovskite, Appl. Catal. B Environ. 125 (2012) 418–424, https://doi.org/10.1016/j.apcatb.2012.06.015.

[100] M.M. Dávila-Jiménez, M.P. Elizalde-González, E. García-Díaz, M. González, M.E. Mendoza, M.J. Robles-Águila, Carbofuran degraded by iron-doped anatase: Weakening the cholinesterase inhibitory activity in the photoproducts mixture, J. Environ. Sci. Heal. - Part B Pestic. Food Contam. Agric. Wastes. 52 (2017) 538–546. https://doi.org/10.1080/03601234.2017.1316161.

[101] S. Sasi, M.P. Rayaroth, D. Devadasan, U.K. Aravind, C.T. Aravindakumar, Influence of inorganic ions and selected emerging contaminants on the degradation of Methylparaben: A sonochemical approach, J. Hazard. Mater. 300 (2015) 202–209, https://doi.org/10.1016/j.jhazmat.2015.06.072.

[102] B. Lopez-Alvarez, R.A. Torres-Palma, G. Peñuela, Solar photocatalitycal treatment of carbofuran at lab and pilot scale: Effect of classical parameters, evaluation of the toxicity and analysis of organic by-products, J. Hazard. Mater. 191 (2011) 196–203, https://doi.org/10.1016/j.jhazmat.2011.04.060.

[103] D. Mohanta, M. Ahmaruzzaman, Facile fabrication of novel $Fe_3O_4\text{-}SnO_2\text{-}gC_3N_4$ ternary nanocomposites and their photocatalytic properties towards the degradation of carbofuran, Chemosphere. 285 (2021) 131395, https://doi.org/10.1016/j.chemosphere.2021.131395.

[104] M. Gar Alalm, S. Ookawara, D. Fukushi, A. Sato, A. Tawfik, Improved WO_3 photocatalytic efficiency using ZrO_2 and Ru for the degradation of carbofuran and ampicillin, J. Hazard. Mater. 302 (2016) 225–231. https://doi.org/10.1016/j.jhazmat.2015.10.002.

[105] S. Li, Z. Liu, Z. Qu, C. Piao, J. Liu, D. Xu, X. Li, J. Wang, Y. Song, An all-solid-state Z-scheme $NaNbO_3\text{-}Au\text{-}Sn_3O_4$ photocatalyst for effective degradation of carbofuran under sunlight irradiation, J. Photochem. Photobiol. A Chem. 389 (2020) 112246, https://doi.org/10.1016/j.jphotochem.2019.112246.

[106] H. Yang, S. Zhou, H. Liu, W. Yan, L. Yang, B. Yi, Photocatalytic degradation of carbofuran in TiO_2 aqueous solution: Kinetics using design of experiments and mechanism by HPLC/MS/MS, J. Environ. Sci. (china) 25 (2013) 1680–1686, https://doi.org/10.1016/S1001-0742(12)60217-4.

[107] J. Fenoll, P. Hellín, P. Flores, C.M. Martínez, S. Navarro, Degradation intermediates and reaction pathway of carbofuran in leaching water using TiO_2 and ZnO as photocatalyst under natural sunlight, J. Photochem. Photobiol. A Chem. 251 (2013) 33–40, https://doi.org/10.1016/j.jphotochem.2012.10.012.